Formulating the interacting boson model by mean-field methods

Kosuke Nomura,[1] Noritaka Shimizu,[1] and Takaharu Otsuka[1,2,3]

[1]*Department of Physics, University of Tokyo, Hongo, Bunkyo-ku, Tokyo, 113-0033, Japan*

[2]*Center for Nuclear Study, University of Tokyo, Hongo, Bunkyo-ku Tokyo, 113-0033, Japan*

[3]*National Superconducting Cyclotron Laboratory, Michigan State University, East Lansing, Michigan, USA*

(Received 23 November 2009; revised manuscript received 17 March 2010; published 12 April 2010)

The interacting boson model (IBM) Hamiltonian is determined microscopically for general cases of low-lying quadrupole collectivity. Under the assumption that the multinucleon-induced surface deformations, which reflect nuclear forces and the Pauli principle, can be simulated by bosons, the interaction strengths of the IBM Hamiltonian are derived by mapping the potential energy surface of the mean-field model with Skyrme force onto the corresponding one of the IBM. These interaction strengths turn out to change gradually as functions of valence nucleon numbers. The energy eigenvalues and the wave functions are calculated with the exact treatment of the particle number and the angular momentum. We demonstrate how well the method works by taking Sm isotopes as an example, where a typical spherical-deformed shape-phase transition is reproduced successfully. We show that the physically relevant IBM interaction strengths can be determined unambiguously by the use of wavelet analysis. In addition, by the diagonalization of the boson Hamiltonian, quantum-mechanical correlation effects can be included in the eigenenergies, by which the basic properties of these nuclei are properly reproduced. The present method is applied to several other isotopic chains, Ba, Xe, Ru, Pd, W, and Os, in comparison to the experimental data. We point out the relevance of our results to the recently proposed critical-point symmetries. The predicted spectra and the B(E2) ratios are presented for heavy neutron-rich exotic nuclei in experimentally unexplored regions such as the right-lower corner of ^{208}Pb on the nuclear chart.

DOI: 10.1103/PhysRevC.81.044307 PACS number(s): 21.10.Re, 21.60.Ev, 21.60.Fw, 21.60.Jz

I. INTRODUCTION

The atomic nucleus exhibits the feature of collective motion induced by the dynamics of all the constituent nucleons. The collective motion is closely linked to the low-energy surface deformation, which generates change in the density distributions in a given nucleus, resulting in a variety of the deformations of nuclear shape from the sphere: the rotation of the deformed ellipsoid, the oscillation of the surface, and the situations in between. Such a deformed nuclear system as a whole carries angular momentum and exhibits in, e.g., its excitation spectra and transition strengths, a certain class of regularities, where one of the most prominent aspects is of a quadrupole nature, namely the quadrupole collectivity. The quadrupole collective motion is of much importance in the structures of both stable and exotic nuclei and has been a central concern in nuclear physics [1,2].

The interacting boson model (IBM) of Arima and Iachello [3,4] has been successful for the phenomenological description of the low-lying collective states for medium-heavy and heavy nuclei. The main ansatz is to employ bosons, which are supposed to simulate the motion of the collective nucleon pairs coupled to angular momentum $J^\pi = 0^+$ (s bosons) and 2^+ (d bosons) with the basic interactions between them [5,6]. The IBM embodies an entire class of symmetries and regularities of the low-lying quadrupole collective states: three dynamical symmetries, U(5) [7], SU(3) [8], and O(6) [9] limits, where the boson Hamiltonian can be written in some specific forms based on simple algebraic relations, and the intermediate situations of these limits, to which most realistic nuclei belong. The IBM in its earliest version (referred to as IBM-1) is purely phenomenological so that the interaction strengths of the model Hamiltonian have been determined from experiment or taken from earlier fitting calculations. Therefore, the IBM itself needs a certain microscopic foundation starting from the nucleonic degrees of freedom.

The IBM is essentially a vast truncation of the nuclear shell model, where the so-called proton s_π and d_π bosons and neutron s_ν and d_ν bosons reflect collective pairs of valence protons, S_π and D_π, and neutrons, S_ν and D_ν, respectively [5,6,10]. As the numbers of valence protons and neutrons are constant for a given nucleus, the numbers of proton and neutron bosons, denoted respectively by n_π and n_ν, are set equal to half of the valence proton and neutron numbers. The interaction strengths of the boson Hamiltonian have been determined by the mapping from the SD subspace of the full shell-model space onto the sd boson space. The mapping scheme for deriving the IBM Hamiltonian of this type is usually referred to as the Otsuka-Arima-Iachello (OAI) mapping and can be extended as the proton-neutron interacting boson model (IBM-2) as a natural consequence [5,6]. The OAI mapping has been practiced for limited realistic cases of nearly spherical or γ-unstable shapes [11–14] by using zero- and low-seniority states of the shell model [5,6,10] and has been also tested for deformed Sm isotopes by renormalizing the contribution from the G pairs as a perturbation [15]. A fermion-boson mapping for deformed nuclei has been studied partly by the "independent-pair" property of condensed coherent fermion pairs [16] and by the rotation of the intrinsic state (a state in the body-fixed frame) [17]. In addition, there are many systematic calculations within the IBM-2 phenomenology for, e.g., Xe-Ba-Ce [18], Ru-Pd [19], Kr [20], and W-Os [21,22] regions. The microscopic basis of the IBM has been questioned

for many years, but is still open for the cases involving the strongly deformed nuclei.

One of the most successful and well-established mean-field models of nuclei is of the Skyrme-type, which have been useful for the description of various intrinsic-state properties of a nucleus: mass, density distributions, surface deformation, etc. [2,23–25]. While a given Skyrme interaction appears to give a basic and systematic description of matter and bulk properties of almost all nuclei on the nuclear chart, it has not been so easy in general to calculate levels and wave functions of excited states with the precise treatment of the particle number and the angular momentum. This is due not only to numerical difficulties but also to methodological problems, as pointed out in Ref. [26].

Here we note that considerable effort has been made for the purpose of nuclear spectroscopy by many studies beyond the mean field, such as those with the generator coordinate method (GCM). GCM has been applied, e.g., starting with the Skyrme density functional, to axially symmetric [27] and triaxial [28] configurations to calculate and to predict the excitation spectra and transition probabilities and to the global studies of correlation effects in the ground state of even-even nuclei [29]. While fundamental problems frequently occur when using a general density functional beyond the mean field, a possible way to regularize them has been investigated [30].

In addition, there have been studies to derive a collective model Hamiltonian from mean-field calculation with, e.g., Skyrme force, to obtain spectroscopic observables. For instance, P. Bonche *et al.* derived, starting from the GCM kernels [31], a collective Bohr Hamiltonian in a one-dimensional case. While this may remain to be generalized, a further study has been carried out in a more accurate manner [29].

Recently, we have proposed an entirely new scheme to determine a Hamiltonian of the IBM(-2) microscopically for general cases [32]. The mean-field potential energy surface (PES) is mapped onto the corresponding PES of the boson system to yield the interaction strengths of the IBM Hamiltonian. A state on the mean-field PES is considered to be a starting point because it has a rather direct relevance to the quadrupole deformation and appears to be suitable for constructing a model of Hamiltonian for the description of the low-lying collective states. By constructing the IBM Hamiltonian based on the mean-field models, utilizing the merits of both schemes, one is able to obtain the energy eigenvalues and the wave functions including those for unexplored regions. Note that, in this work, the IBM stands as it has been without changing its basic framework such as the boson number counting rule and its algebraic features.

In the preceding Letter [32], we put much emphasis on the basic idea of this approach, ending up with only a few key results rather than the systematic calculations in comparison to the experiments. In addition, it remains to be fully discussed that the IBM interaction strengths can be determined rather unambiguously. The aim of the present article is to give detailed explanations of the above-mentioned problems.

The article is organized as follows: In Sec. II, the formalism and the underlying physical interpretation of the mapping procedure are sketched. In Sec. III we demonstrate how the IBM parameters can be determined in practice, taking the transition from spherical to deformed shapes in Sm isotopes as an example. Systematic behaviors of the excitation spectra and the $E2$ transition strength [B(E2) ratio] are studied. We demonstrate that the IBM interaction strengths can be determined quite unambiguously by the use of the wavelet analysis. The present method is applied to evaluate the correlation energy in the ground state, which is a natural consequence of the quantum-mechanical calculations by the IBM. In Sec. IV, the calculated results for Ba, Xe, Ru, and Pd isotopes within the $N = 50$–82 major shell are presented and are compared with the experiments. We will then report the predicted spectra and B(E2) ratios of neutron-rich exotic nuclei, namely W and Os isotopes with $N > 126$, for which no experimental data are available. A summary and concluding remarks will be presented in Sec. V.

II. THEORETICAL PROCEDURE

A. The mean-field PES

We start from the constrained Skyrme Hartree-Fock plus BCS calculations in a usual way [2] to obtain the PES (denoted by HF PES) in terms of the deformation variables $\beta_{\rm F}$ and $\gamma_{\rm F}$, which imply geometrical deformation parameters [1].

The EV8 code is used, where the single-particle wave functions are represented by a three-dimensional Cartesian grid and are assumed to be symmetric with respect to x-y-z planes [33,34]. We use a mesh spacing of 0.8 fm throughout. We use the Skyrme SLy4 [35] and SkM* [36] interactions, while the following results do not depend too much on the choice of Skyrme parametrizations as long as the usual ones are taken.

The quadratic constraint is imposed on the Skyrme mean-field calculation in such a way as to add the potential term $\sum_{m=0,2} C_m(\langle\hat{Q}_{2m}\rangle - \mu_m)^2$ to the Hamiltonian. Here, $\langle\hat{Q}_{2m}\rangle$ stands for the expectation value of a component of the mass quadrupole moment $\hat{Q}_{2m} = r^2 Y_{2m}$. Here C_m and μ_m represent the strength of the constraint and some desired value for the quadrupole deformation of interest, respectively. In order to draw the PES in a usual β-γ plane, the triaxial degree of freedom is introduced as

$$\begin{aligned} \beta_F &= \sqrt{\frac{5}{16\pi}}\frac{4\pi}{3}\frac{1}{A(r_0A^{1/3})^2}q_0 \\ \gamma_{\rm F} &= \tan^{-1}\left(\sqrt{2}\frac{\langle\hat{Q}_{22}\rangle}{\langle\hat{Q}_{20}\rangle}\right) \end{aligned} \tag{1}$$

with $r_0 = 1.2$ fm and $q_0 \equiv \sqrt{\langle\hat{Q}_{20}\rangle^2 + 2\langle\hat{Q}_{22}\rangle^2}$. It is sufficient to consider the problem in the range $0^\circ \leqslant \gamma_{\rm F} \leqslant 60^\circ$ since in the quadrupole deformation the nuclear shape remains unchanged under the interchange of all three axes of the intrinsic frame.

We use the density-dependent zero-range type of the pairing interaction, which is truncated both below and above the Fermi surface by 5 MeV for both protons and neutrons. The fixed value -1250 MeV fm^3 is used for the strength of the pairing force throughout the calculations. In addition,

the Lipkin-Nogami prescription [37–39] is employed for the treatment of the particle number.

B. The IBM PES

We turn to the IBM description of the PES. In this study we discuss the IBM-2 because it is close to a microscopic picture, compared to a simpler version of the IBM. The following standard IBM-2 Hamiltonian is employed

$$\hat{H}_{\rm tot} = E_0 + \hat{H}_{\rm IBM} \tag{2}$$

with

$$\hat{H}_{\rm IBM} = \epsilon(\hat{n}_{d\pi} + \hat{n}_{d\nu}) + \kappa\,\hat{Q}_\pi \cdot \hat{Q}_\nu, \tag{3}$$

where E_0 is a constant for a given nucleus and will be taken into account in Sec. III E. Note that E_0 does not change the excitation energies. The first term on the right-hand side of Eq. (3) stands for the d-boson number operator,

$$\epsilon\hat{n}_{d\rho} = \epsilon d^\dagger_\rho \tilde{d}_\rho \ (\rho = \pi \text{ or } \nu), \tag{4}$$

with ϵ denoting the single d-boson energy relative to the s boson one. This term with $\epsilon > 0$ contributes to keeping a nucleus spherical. $d^\dagger_\rho \cdot \tilde{d}_\rho$ is a scalar product, and $\tilde{d}_\rho$ is defined as $\tilde{d}_{\rho\mu} \equiv (-1)^\mu d_{\rho-\mu}$ ($\mu = 0,\pm1,\pm2$). While ϵ can differ between proton and neutron, they are set equal for simplicity. The second term on the right-hand side of Eq. (3) is the quadrupole-quadrupole interaction between proton and neutron bosons with the strength κ, inducing the quadrupole deformation. The parameters $\chi_{\pi,\nu}$ appear as

$$\hat{Q}_\rho = [s^\dagger_\rho \tilde{d}_\rho + d^\dagger_\rho \tilde{s}_\rho]^{(2)} + \chi_\rho [d^\dagger_\rho \tilde{d}_\rho]^{(2)} \tag{5}$$

with $\tilde{s}_\rho \equiv s_\rho$ and determine the prolate or oblate shape of deformation, reflecting the structure of collective nucleon pairs as well as the numbers of valence nucleons [5,6,10].

The IBM system of interest is connected to a certain geometrical picture by introducing the boson coherent state [40–42], defined as

$$|\Phi\rangle \propto \prod_{\rho=\pi,\nu} \left[s^\dagger_\rho + \sum_{\mu=0,\pm2} \alpha_{\rho\mu} d^\dagger_{\rho\mu} \right]^{n_\rho} |0\rangle, \tag{6}$$

where $|0\rangle$ stands for the boson vacuum (i.e., inert core) and α's are amplitudes expressed more transparently as $\alpha_{\rho0} = \beta_\rho \cos\gamma_\rho$, $\alpha_{\rho\pm1} = 0$ and $\alpha_{\rho\pm2} = \frac{1}{\sqrt{2}}\beta_\rho \sin\gamma_\rho$, where β_ρ and γ_ρ are called intrinsic variables. The β's represent the relative d-boson probability amplitude over the s boson. As the s boson can create only a spherical state and the description of the quadrupole deformation requires the d boson, the β's are parameters indicating the quadrupole deformation. The coherent state $|\Phi\rangle$ represents an intrinsic state. If the quadrupole deformation has an axial symmetry, one can choose the z axis to be the symmetry axis. In this case, the coherent state must be invariant with respect to the rotation about the z axis. This leads us to $\alpha_{\rho2} = \alpha_{\rho-2} = 0$ or $\gamma_\rho = 0^\circ$ in Eq. (6). A different value of γ indicates a triaxial deformation. Thus, one can describe the (intrinsic) shape of the nucleus in terms of β_ρ and γ_ρ. The former measures the total magnitude of the deformation, while the latter the triaxiality.

In principle, both β_ρ and γ_ρ can take different values for proton and neutron bosons. Since protons and neutrons attract each other strongly, the proton and the neutron systems should have the same shape in the first approximation. We therefore assume that β_π (γ_π) and β_ν (γ_ν) take the same values, denoted by $\beta_{\rm B}$ ($\gamma_{\rm B}$), for proton and neutron bosons,

$$\begin{aligned} \beta_\pi &= \beta_\nu \equiv \beta_{\rm B} \\ \gamma_\pi &= \gamma_\nu \equiv \gamma_{\rm B}. \end{aligned} \tag{7}$$

The range of $\gamma_{\rm B}$ is set $0^\circ \leqslant \gamma_{\rm B} \leqslant 60^\circ$, as for $\gamma_{\rm F}$.

In the following, the expectation value of an operator $\hat{O}$ with respect to $|\Phi\rangle$ is denoted by $\langle\hat{O}\rangle \equiv \langle\Phi|\hat{O}|\Phi\rangle/\langle\Phi|\Phi\rangle$ unless otherwise specified. To calculate the bosonic PES (referred to as IBM PES, hereafter), IBM-2 Hamiltonian of Eq. (3) is substituted to $\hat{O}$. Similarly to the IBM-1 case [43], the IBM PES can be calculated straightforwardly to have the analytical form as

$$\begin{aligned} \langle\hat{H}_{\rm IBM}\rangle = {} & \frac{\epsilon(n_\pi + n_\nu)\beta_{\rm B}^2}{1+\beta_{\rm B}^2} + n_\pi n_\nu \kappa \frac{\beta_{\rm B}^2}{\left(1+\beta_{\rm B}^2\right)^2} \\ & \times \left[4 - 2\sqrt{\frac{2}{7}}(\chi_\pi + \chi_\nu)\beta_{\rm B}\cos 3\gamma_{\rm B} + \frac{2}{7}\chi_\pi\chi_\nu\beta_{\rm B}^2 \right], \end{aligned} \tag{8}$$

which covers all geometrical pictures associated with three dynamical symmetries of the IBM, namely spherical, axially symmetric deformed, and γ-unstable shapes. Note that, however, neither of the coexisting and the triaxial minima can be described by the IBM PES in the present case.

C. Mapping of the PES's

While the deformation variables β and γ could be in principle different between fermion and boson systems, they can be related to each other. $\beta_{\rm B}$ is related to $\beta_{\rm F}$ in the following way. For axially symmetric deformation ($\gamma_{\rm B} = 0^\circ$), the intrinsic quadrupole moment Q_I can be defined as $Q_I = q\langle\hat{Q}_\pi + \hat{Q}_\nu\rangle$, where q is an overall scaling factor. Q_I is calculated as

$$Q_I = \frac{q\left[2(n_\pi + n_\nu)\beta_{\rm B} - \sqrt{\frac{2}{7}}(n_\pi\chi_\pi + n_\nu\chi_\nu)\beta_{\rm B}^2\right]}{1+\beta_{\rm B}^2}. \tag{9}$$

In the present study, the typical range of $\beta_{\rm B}$ is $0 \leqslant \beta_{\rm B} \lesssim 1$. Also practically, $|\chi_{\pi,\nu}| \lesssim 1$ is fulfilled. Thus, the term proportional to $\beta_{\rm B}^2$ in Q_I becomes minor as compared to the rest and is neglected in the first approximation. This leads us to $\beta_{\rm B} \propto \beta_{\rm F}$, because $\beta_{\rm F}$ is proportional to Q_I, which is associated with q_0 of Eq. (1) when the axial symmetry is assumed.

We now assume the separability of the mapping of β and that of γ, for simplicity. Another variable $\gamma_{\rm B}$ can then be equated to $\gamma_{\rm F}$, again for simplicity, as both of them should be limited to the 0° to 60° interval. We therefore have

$$\begin{aligned} \beta_{\rm B} &= C_\beta \beta_{\rm F} \\ \gamma_{\rm B} &= \gamma_{\rm F}, \end{aligned} \tag{10}$$

where C_β is the scale factor, characterizing the proportionality relation between β's. Note that C_β may vary from nucleus to another gradually as a function of n_π and n_ν.

Once the HF PES is obtained, we map a point on it onto the corresponding point on the IBM PES. This is exactly a mapping of the mean-field state at (β_F, γ_F) on the PES onto the corresponding IBM state at (β_B, γ_B). We actually determine the values of the five parameters, ϵ, κ, $\chi_{\pi,\nu}$, and C_β, for each individual nucleus by drawing the IBM PES with the formulas of Eqs. (8) and (10) so as to reproduce the overall shape of the HF PES. The overall shape is in this case characterized by the location $(\beta_F,\gamma_F) = (\beta_{min},\gamma_{min})$ at which the minimum occurs in the HF PES, and the curvatures (not at a particular point) for both β and γ directions. In determining such parameters, special attention has to be paid to their gradual systematic changes with valence nucleon numbers, reflecting a gradual growth of deformation. The scale factor C_β is mainly determined by adjusting (β_{min}, γ_{min}) and the curvature in β direction of the IBM PES to those of the HF PES. ϵ and κ are mainly determined as functions of n_π and n_ν so as to reproduce the depth of the potential in β direction, namely the energy difference between the configurations $\beta_F = \beta_{min}$ and $\beta_F = 0$ with $\gamma = \gamma_{min}$. As the γ dependence of the IBM PES of Eq. (8) appears as the term proportional to $\cos 3\gamma_B$, the curvature of the HF PES in γ direction can be reproduced by tuning the value of the quantity $\chi_\pi + \chi_\nu$, which also determines, depending on its sign, either a prolate or oblate minimum of the IBM PES. χ_π and χ_ν are obtained as functions of n_π and n_ν, respectively.

As an example, we show in Fig. 1 the HF and the IBM PES's for Sm isotopes calculated with the Skyrme SLy4 force.

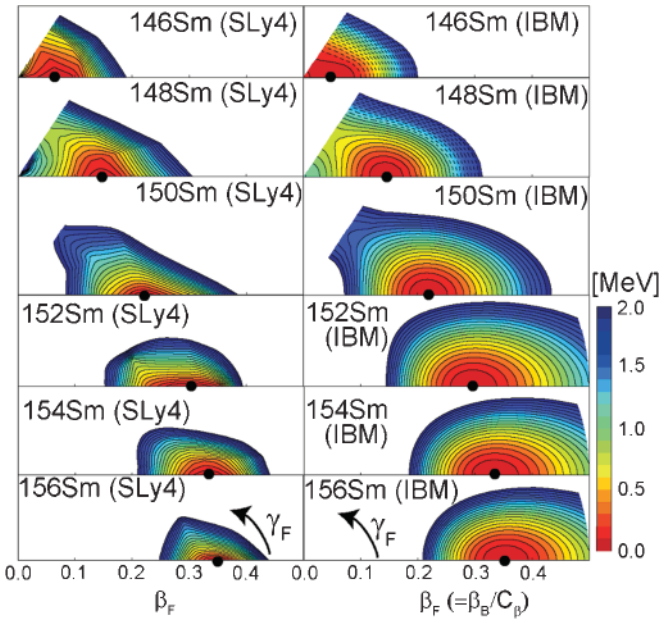

FIG. 1. (Color online) The potential energy surfaces (PES's) of the HF and the IBM up to 2 MeV excitation from the energy minimum, studied with Skyrme SLy4 force for Sm isotopes. The coordinate β_B (γ_B) of the IBM PES is expressed in terms of β_F (γ_F) using the formula of Eq. (10). γ_F is limited to 0° to 60°. Contour spacing is 100 keV and minima can be identified by the solid circles.

The PES's are depicted in contour plots within the excitation of 2 MeV in energy measured from the potential minimum. The coordinate β_B (γ_B) of the IBM PES is expressed in terms of β_F (γ_F), for simplicity, using the formula of Eq. (10). In the following we shall show the PES's up to 2 MeV excitation since the low-lying collective states are supposed to be dominant in this range.

Note that χ-square fit may not make much sense because the present IBM Hamiltonian of Eq. (3) is rather simple. Thus, we take the global pattern of the PES rather than the local one like the curvature at a particular point. The overall pattern of the HF PES reflects how nuclear force and the Pauli principle work in determining the energy of the collective state over the relevant range of shapes. By reproducing the overall pattern of the HF PES as much as possible, the boson system is expected to simulate, to a good extent, such basic properties of nuclear system in a simple manner. With the optimal set of the parameters thus obtained, we diagonalize the boson Hamiltonian of Eq. (3) with the NPBOS code [44] to yield the levels and the wave functions having good quantum numbers in the laboratory system. In addition, as we will show, the diagonalization may include to a good extent the quantum effect on the eigenenergy, which cannot be taken into account at the mean-field level.

Here we point out that a general boson Hamiltonian may contain some interaction terms which affect levels but cannot be determined by simply comparing the PES's. Strengths of such interactions can be determined by making some higher-order corrections, e.g., cranking of a strongly deformed object. In this case the response of the nucleonic system may need to be treated well by the IBM. A mapping scheme of this kind may become necessary for further refinement, which is beyond the scope of the present article. The Hamiltonian $\hat{H}_{IBM}$ of Eq. (3) is, although being simple, assumed to be an essential part of a general IBM Hamiltonian to describe the properties of the quadrupole collective states.

Moreover, in some microscopic approaches of the collective model, the PES is treated as an effective potential, and a generalized kinetic term (or mass parameter) is introduced to obtain excitation levels. We point out that in the present work the total energy of the HF-BCS is compared with the corresponding energy of the IBM. In this case, the mass parameter itself is not considered explicitly, while its effect is, mainly for spherical and weakly deformed nuclei, supposed to be included to a certain extent in the diagonalization of the boson Hamiltonian calibrated by the comparison of PES's.

III. DERIVATION OF THE IBM PARAMETERS: SAMARIUM ISOTOPES AS AN EXAMPLE

A. PES's and derived IBM parameters

We shall now illustrate the mapping procedure by taking Sm isotopes as an example. For the sake of completeness we also show the result studied with Skyrme SkM*, in addition to the SLy4 result, whose PES has appeared in Fig. 1. Note that the result with the SLy4 force is the refinement of our earlier calculation [32], while the qualitative picture remains the same. We also note that the deformation parameter β (γ)

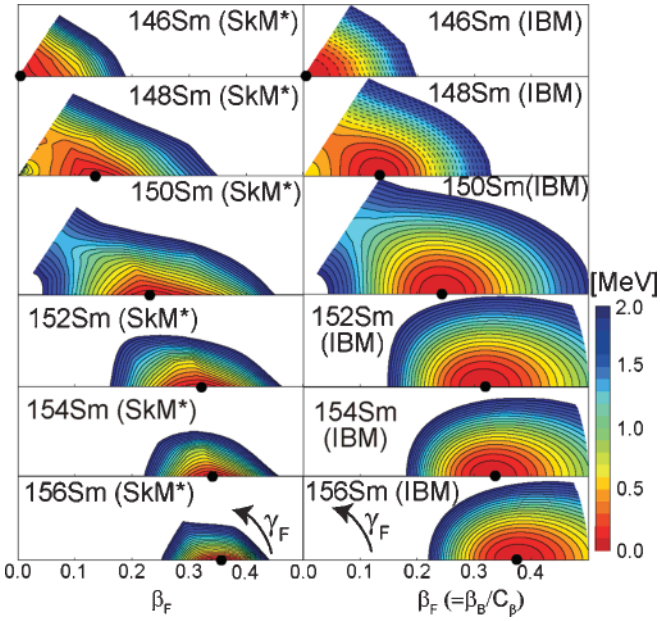

FIG. 2. (Color online) Same as Fig. 1 but for SkM*.

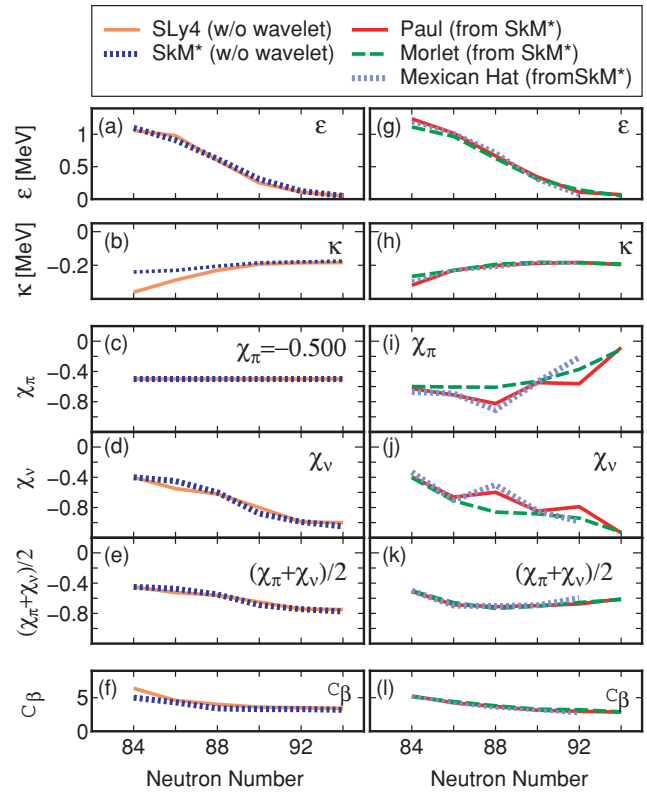

FIG. 3. (Color online) (a)–(f) Evolution of the IBM parameters for Sm isotopes as functions of N. The wavelet analysis has not been performed. The Skyrme SLy4 (solid curve) and SkM* (dotted curve) forces are used. The fixed value $\chi_\pi = -0.500$ is used for both Skyrme forces. (g)–(l) Evolution of the optimized parameters by the wavelet analysis, which are discussed in Sec. III C. The Paul (solid curve), Morlet (dashed curve), and Mexican hat (dotted curve) wavelet functions are used.

that appears in the following always means β_F (γ_F), unless otherwise specified.

Figures 1 and 2 show that both Skyrme forces give similar PES, while there exist certain differences particularly in the transitional region. One can find abrupt changes of HF PES from $N = 86$ to 88 for the SLy4 case and from $N = 88$ to 90 for the SkM*. For $N = 84$ and 86, one also finds a difference between the SLy4 and SkM* cases, namely the former is steeper than the latter. With the increase of the neutron number, N, the HF PES becomes steeper in both β and γ directions and $\beta_{\min}$ shifts away from the origin, resulting in strong prolate deformation for larger N. ^{148}Sm has been recognized as an example of the spherical vibrator, being close to U(5) limit of IBM. The HF PES of the present calculation for ^{148}Sm somewhat differs from this picture, placing the energy minimum at $\beta \sim 0.15$. The IBM PES reproduces $\beta_{\min}$ and the overall pattern of the HF PES. In the vicinity of SU(3) limit, ^{154}Sm, HF PES has a pronounced sharp minimum, and IBM PES also exhibits a similar one. The minimum valley is, however, shallower for the IBM PES. This is a general trend that cannot be changed any more by simply playing with parameters and is probably due to the finite number and/or limited types of bosons.

We show in Figs. 3(a)–3(f) the evolution of the derived parameters of the IBM Hamiltonian as functions of N. In general ϵ and χ_ν vary rather significantly, while κ and C_β change much less.

In Fig. 3(a) ϵ becomes smaller with N similarly to the earlier phenomenological study [45]. The gradual decrease of ϵ with N has been discussed in a microscopic picture [16] as a consequence of stronger coupling between "unperturbed d boson" and other types of bosons such as the one with spin 4 [or g boson] [5,6,46].

In Fig. 3(b), the magnitude of κ is in general set somewhat large in comparison to the phenomenological value [45] and OAI result [15]. This indicates that the present HF PES for Sm isotopes exhibits a too deep potential valley to be reproduced by the IBM PES with the phenomenological value of κ. For $N = 84$ and 86, κ of SLy4 deviates significantly from that of SkM*, reflecting the difference of the PES between SLy4 and SkM*.

As seen from Fig. 3(c), a common value of χ_π ($= -0.500$) is assumed for simplicity in both SLy4 and SkM* results, similarly to earlier works [5,6,10]. In Fig. 3(d), χ_ν has a rather strong dependence on N and changes at $N = 88$ or 90, reflecting the structural evolution from transitional to deformed shapes. The seniority prescription in the OAI mapping [5,6] gives the opposite dependence of χ_ν on N, while the present one appears to be consistent with a mapping method using deformed intrinsic states [16]. The average $(\chi_\pi + \chi_\nu)/2$ is also shown in Fig. 3(e), which will be discussed in Sec. III C in comparison to the wavelet results.

The scale factor C_β in Fig. 3(f) becomes smaller in smooth systematics with N, reflecting the gradual shift of $\beta_{\min}$. In Fig. 3(f), for deformed nuclei with $N \geqslant 92$, the value of C_β satisfies that $C_\beta \beta_{\min}$ is smaller than $\sqrt{2}$, at which the minimum occurs in SU(3) limit with $n_\rho \to \infty$ [40–42].

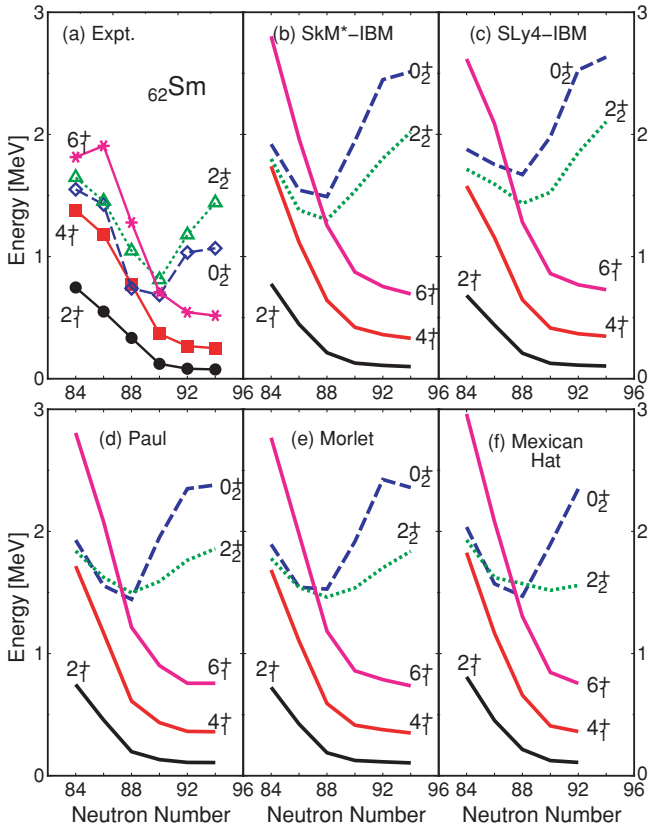

FIG. 4. (Color online) Low-lying spectra for Sm isotopes as functions of N. Upper panel: (a) the experimental [47] and calculated levels with Skyrme (b) SkM* and (c) SLy4 forces. Lower panel: Results from the wavelet analysis (discussed in Sec. III C) using (d) Paul, (e) Morlet, and (f) Mexican hat wavelets.

B. Spectra

In Fig. 4 we show the low-lying spectra for Sm isotopes with $N = 84$–94 as functions of N. The experimental spectra are shown in Fig. 4(a), in which each data is connected by a line. Figures 4(b) and 4(c) show the calculated results for SLy4 and SkM* interactions, respectively, using the derived parameters in Figs. 3(a)–3(f). Figures 4(d)–4(f) show the results using the IBM parameters determined by the wavelet analysis, which is discussed in the next section.

At both $N = 84$ and 86 in Figs. 4(b) and 4(c), the calculated spectra exhibit U(5)-like features: 4_1^+, 2_2^+, and 0_2^+ states form a triplet. However, this is not the case with the experimental data for $N = 84$, in which 6_1^+ state is lying close to 4_1^+, 2_2^+, and 0_2^+ states. For $N = 86$, the calculated levels are fairly close to the experimental data. With the increase of N, each calculated level comes down consistently with the experimental trends particularly for the yrast levels.

As suggested by the experiments, there should be a critical point at $N = 90$, beyond which the 2_2^+ and 0_2^+ levels turn to go up. In Figs. 4(b) and 4(c) the sharp increases of the calculated side-band levels occur at $N = 88$ rather than at $N = 90$. For $N \geqslant 92$, one sees rotational spectra. The OAI mapping for Sm isotopes [15], where the collective G pair is renormalized perturbatively, gives similar results, but the present calculation seems to better reproduce the trends of the side-band levels, including their transitional behaviors.

The level evolution in Figs. 4(a)–4(c) shows properties of X(5) critical-point symmetry [48–50] around $N = 88$ or 90, while the $N = 88$ nucleus is closer to X(5) in the present work. In fact, the calculated values of the ratio $R_{4/2} \equiv E(4_1^+)/E(2_1^+)$ for $N = 88$ and 90 for SLy4 (SkM*) force are 3.09 (3.01) and 3.30 (3.30), respectively. The experimental value for ^{152}Sm and the X(5) value are 3.01 and 2.91, respectively. This deviation may be due to the properties of the HF PES's in Figs. 1 and 2, which do not identify a specific nucleus as the critical point.

The calculated excitation levels for $N \geqslant 90$ are higher than the experimental [47] and the phenomenological [45] ones, although the overall pattern characterized, e.g., by the ratios between levels, is reproduced fairly well with a clear signature of the spherical-deformed shape phase transition. This problem seems to be seen in many GCM results [51] for strong deformation, although it does not show up for moderately deformed cases.

C. Wavelet analysis

As we have discussed in Sec. III A, the physically relevant IBM parameters can be derived so that the IBM PES reproduces the HF PES as much as possible. In the present case, however, the χ-square fit turns out to be unfeasible because of some local patterns of the HF PES. It may be questioned whether the physically relevant IBM parameters can be determined unambiguously. In the following we shall focus on this problem.

We employ the wavelet analysis, which has been developed in the field of signal processing (for reviews, see Refs. [52,53], for instance) and also applied to a physical system [54]. A given signal is transformed into a set of coefficients (wavelet transform) using an appropriate basis function (a wavelet function or a so-called wavelet), which is localized both in time and frequency domains. In the present case, the wavelet transform of the PES can be characterized by the deformation variable β (γ) and its scale parameter $\delta\beta$ ($\delta\gamma$), which, in the terminology of the signal processing, correspond respectively to time and frequency. The wavelet function (denoted by Ψ) satisfies the conditions that it has zero mean and that it is square integrable, which mean that Ψ must oscillate in a finite duration. These conditions allow one to analyze efficiently the localized signal, some part of which is particularly important like the relevant low-energy region of the PES. In addition, one is able to choose a wavelet which appears to be suited well for extracting a characteristic feature of the signal in question. These flexibilities make the wavelet analysis distinct from the Fourier transform, which localizes only frequency with a limited use of a basis function.

For precise analysis, the continuous wavelet transform is carried out in the present work. The wavelet transform of the PES in β direction (for fixed γ) is formulated as

$$\tilde{E}(\delta\beta, \beta) = \frac{1}{\sqrt{\delta\beta}} \int E(\beta', \gamma) \Psi^{\star} \left(\frac{\beta - \beta'}{\delta\beta} \right) d\beta', \qquad (11)$$

where $\Psi^\star$ is a complex conjugate of a wavelet function. $E(\beta', \gamma)$ stands for the PES of either the HF or the IBM, while $\tilde{E}(\delta\beta, \beta)$ is its wavelet transform and is in general a complex value. For the γ direction, one has only to replace β ($\delta\beta$) with γ ($\delta\gamma$) in Eq. (11). Note that the wavelet transform is done separately for β and γ directions because the integral in Eq. (11) is defined in one dimension.

One should in general choose a wavelet function Ψ having a somewhat similar shape as the original signal. Then, we employ the following wavelet functions, which are frequently used [52,53]: (i) Mexican hat (second derivative of the Gaussian function), $\Psi(x) = (1 - x^2)\exp(-\frac{x^2}{2})$; (ii) Morlet, $\Psi(x) = \pi^{-1/4} e^{ikx} \cdot e^{-x^2/2}$; and (iii) Paul, $\Psi(x) = 2^m i^m m!(1 - ix)^{-(m+1)}/\sqrt{\pi(2m)!}$, where integers k and m are control parameters and are set as $k = 6$ and $m = 4$, respectively, for practical reasons. These wavelets exhibit in common an oscillation within a Gaussian-like envelope.

The integration in Eq. (11) is performed by means of the fast Fourier transform [53] within the appropriate range of β' (or γ'), i.e., the relevant range of low-energy (several MeV) excitation. For strongly deformed nuclei, the integration range in β direction should be as small as possible and should include $\beta_{\min}$. Otherwise one ends up with some unfavorable parameter values which, even though giving good fits, do not make much physical sense.

In addition, one is able to reconstruct the original signal out of $\tilde{E}(\delta\beta, \beta)$ in Eq. (11) in order to ensure the wavelet transform is done properly. For fixed γ, the reconstructed PES is written as

$$E(\beta, \gamma) \propto \int\int \frac{\tilde{E}(\delta\beta, \beta')}{(\delta\beta)^{5/2}} \Psi\left(\frac{\beta' - \beta}{\delta\beta}\right) d(\delta\beta) d\beta'. \quad (12)$$

Actually, we first calculate the squared wavelet transform of the IBM PES and fit it to that of the HF PES. Then, we optimize the IBM parameters by the simplex method. Thereby the IBM parameters can be derived without any arbitrariness. For nearly spherical nuclei, the fitting is carried out only along the line of axial symmetry. For deformed nuclei, γ degrees of freedom are also taken into account by minimizing the sum of the χ-square functions for β and γ directions. We use the mesh spacings $\Delta\beta = 0.01$ and $\Delta\gamma = 10^\circ$. In the following, ^{148}Sm and ^{152}Sm nuclei are taken as examples, studied with SkM* force. The Paul wavelet is used. The wavelet transforms are performed for $\gamma = 0^\circ$ in the ranges $-0.29 \leqslant \beta \leqslant 0.29$ for ^{148}Sm and $-0.24 \leqslant \beta \leqslant 0.38$ for ^{152}Sm. For ^{152}Sm the minima on the lines of $\gamma = 10^\circ$, 20°, 30°, 40°, and 50°, in addition to $\gamma = 0^\circ$ and 60°, are also used for the fits.

In each panel of Fig. 5, the squared amplitude $|\tilde{E}|^2$ is drawn in the contour plot for each scale value $\delta\beta$ on the vertical axis and for the β value on the horizontal axis. The left panels of Fig. 5 show the wavelet transforms of the HF PES's (MF-SkM*), while the right panels show the corresponding transforms of the IBM PES's. $|\tilde{E}|^2$ is remarkably large for both nuclei when $\delta\beta$ is of the order of 10^{-1}, where the characteristic features of the PES can be most clearly seen. For the position (β) domain, the location where the amplitude $|\tilde{E}|^2$ becomes largest does not necessarily correspond to the $\beta_{\min}$ of the PES. In fact, for ^{148}Sm (^{152}Sm), $\beta_{\min} \sim 0.15$ (0.32) as one sees

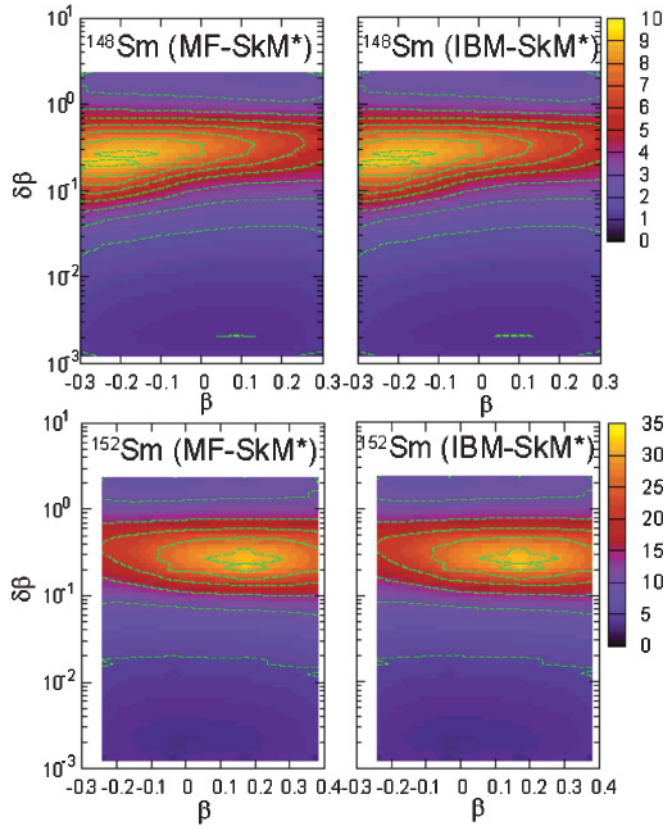

FIG. 5. (Color online) Contour plots of the squared wavelet transforms, the amplitudes $|\tilde{E}|^2$, for the HF and the IBM PES's in β-$\delta\beta$ planes for ^{148,152}Sm. The Paul wavelet is used. Note that the vertical axis is in logarithmic scale.

from Fig. 2, whereas $|\tilde{E}|^2$ is relatively large within the range $-0.30 \lesssim \beta \lesssim -0.10$ ($0.10 \lesssim \beta \lesssim 0.30$) in Fig. 5. However, the pattern of the amplitude $|\tilde{E}|^2$ seems to have a certain relevance to that of the original PES. The magnitude of the former at a point in the position domain appears to reflect the slope of the latter at the corresponding point. The pattern of $|\tilde{E}|^2$ is not strongly affected by the local feature of the PES. Therefore, the PES fit in the wavelet space can be, as expected, good for considering the characteristic, global feature of the PES over the range of interest. By the fit with the wavelet analysis outlined above, the patterns of $|\tilde{E}|^2$s are to every detail in good agreement between HF and IBM for both ^{148}Sm and ^{152}Sm nuclei. Other types of the wavelets give the different pattern of $|\tilde{E}|^2$s from the Paul case, but the major discussion does not change.

In Figs. 6(a) and 6(c), both the original (dashed curves) and the reconstructed (solid curves) HF PES's for ^{148}Sm and ^{152}Sm are depicted in real space. The reconstructed PES is drawn using Eq. (12) with $\gamma = 0^\circ$ and agrees with the original one. This means the wavelet transform is done properly. The corresponding IBM PES's are also shown in Fig. 6(b) ^{148}Sm and 6(d) ^{152}Sm and are compared with the HF PES's. Note that the IBM PES is depicted so that its origin point agrees with the point of the HF PES at the spherical configuration, ($\beta_F = 0, \gamma_F = 0^\circ$). One can see that the HF PES is reproduced nicely by the IBM.

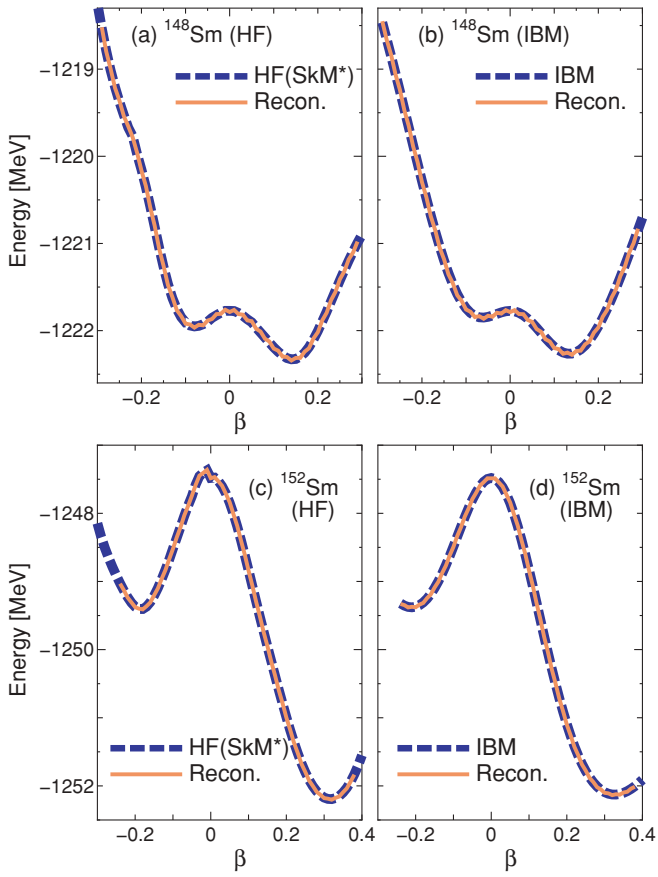

FIG. 6. (Color online) The PES's in the real space. The HF PES's for (a) ^{148}Sm and (c) ^{152}Sm are compared with the IBM PES's for (b) ^{148}Sm and (d) ^{152}Sm, respectively. The reconstructed PES's ("Recon.") are also plotted.

We show on the right-hand-side panels of Fig. 3 the evolution of the IBM parameters for Sm isotopes, derived by the wavelet analysis. The Paul, Morlet, and Mexican hat wavelets are used. The IBM parameters from SkM* force, which appear on the left-hand-side panels of Fig. 3, have been chosen as initial guesses for the simplex method and are hereafter referred to as "w/o-wavelet" parameters, as indicated in the upper panel of Fig. 3. The initial parameters are not chosen arbitrarily but are more or less those close to the w/o-wavelet parameters. This can be tested by using the same w/o-wavelet parameters as initial guesses, one of which is, however, replaced by a different value far from the w/o-wavelet one. In this case, the χ-square fit does not give the global minimum. In addition there may be some other combinations of the IBM parameters which give good fits, but in most cases such parameters do not make much physical sense.

In the present wavelet analysis, we treat χ_π as a free parameter. For $N = 88$–94, fit in the γ direction is also performed. Note that the parameters for the Mexican hat wavelet at $N = 94$ are not shown since the Mexican hat wavelet does not work there. In Figs. 3(g)–3(i), all three wavelet functions give almost identical values of ϵ, κ, and C_β, while χ_π and χ_ν somewhat depend on the wavelets. For Paul and the Mexican hat cases, both χ_π and χ_ν do not evolve smoothly like that for the w/o-wavelet fits, whereas the Morlet wavelet seems to show fairly consistent trends of $\chi_{\pi,\nu}$ with w/o-wavelet results. As one sees from Fig. 3(k), however, the average of χ_π and χ_ν for wavelet calculations has no notable dependence on the choice of the wavelets, while it is less sensitive to N compared to that of the w/o-wavelet calculation. In the future it may be necessary to make it clear why the difference of the local patterns of χ's occurs depending on the choice of the wavelets and to conclude which wavelet is the best for a given physical system. As one sees from the comparisons in Fig. 3, it can be revealed that the optimized parameters by the wavelet analysis are almost the same as the w/o-wavelet ones, except for some local behaviors of the parameters. Some uncertainties of the optimized parameters obviously exist and probably come from either the properties of the wavelet functions or from other choice of the control parameters for numerical use, but they do not affect the resulting levels qualitatively.

The lower panel of Fig. 4 shows the evolution of the calculated excitation spectra with the parameters obtained from the wavelet analyses for (d) Paul, (e) Morlet, and (f) Mexican hat wavelets. Here we emphasize that any of these wavelet functions gives almost the same results to the w/o-wavelet calculation, which is consistent with the experimental trends, including the transitional behaviors.

D. B(E2) ratios

Once the wave functions of the excited states are calculated, one is able to obtain other spectroscopic observables, among which the reduced E2 transition strength B(E2) is of particular importance. It is defined as [1]

$$B(\mathrm{E2}; J \to J') = \frac{1}{2J+1} |\langle J' || \hat{T}^{(\mathrm{E2})} || J \rangle|^2. \tag{13}$$

Here the E2 transition operator $\hat{T}^{(\mathrm{E2})}$ is given by $\hat{T}^{(\mathrm{E2})} = e_\pi \hat{Q}_\pi + e_\nu \hat{Q}_\nu$, where e_ρ represents the boson effective charge. Originally, e_ρ should be determined independently of the mean-field calculation. In the present paper, we assume $e_\pi = e_\nu$, for simplicity, and focus our discussion on the B(E2) ratios defined as follows:

$$\begin{aligned} R_1 &\equiv B(\mathrm{E2}; 4_1^+ \to 2_1^+)/B(\mathrm{E2}; 2_1^+ \to 0_1^+) \\ R_2 &\equiv B(\mathrm{E2}; 2_2^+ \to 2_1^+)/B(\mathrm{E2}; 2_1^+ \to 0_1^+) \\ R_3 &\equiv B(\mathrm{E2}; 0_2^+ \to 2_1^+)/B(\mathrm{E2}; 2_1^+ \to 0_1^+) \\ R_4 &\equiv B(\mathrm{E2}; 2_2^+ \to 0_1^+)/B(\mathrm{E2}; 2_2^+ \to 2_1^+), \end{aligned} \tag{14}$$

which, as we shall show, exhibit the traces of the shape-phase transitions as functions of N.

Figure 7 shows the B(E2) ratios R_1-R_4 for Sm isotopes as functions of N, studied with SLy4 and SkM* forces. Experimental data [55] are also shown. There is no significant difference between SLy4 and SkM* results.

The calculated R_1 value decreases with N and becomes close to the SU(3) limit of the IBM, $R_1 = \frac{10}{7}$ (indicated by dotted line), which is fairly consistent with the experimental data. The calculated values of R_2 and R_3 appear to indicate the transition from spherical to deformed shapes, changing

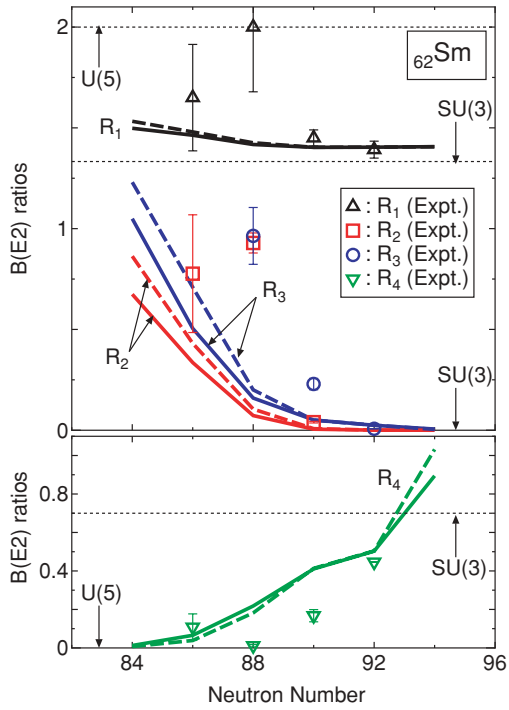

FIG. 7. (Color online) B(E2) ratios for Sm isotopes as functions of N. R_1-R_4 are defined in Eq. (14). Solid and dashed curves stand for the calculated results with SLy4 and SkM* forces, respectively. Data are taken from Ref. [55].

smoothly from around the U(5) limit (=2.00) to the SU(3) limit ($=\frac{10}{7}$), while for the transitional $N = 88$ nucleus, the calculated values are smaller than both the experimental data and the phenomenological value [45].

The calculated R_4 increases as a function of N consistently with the experiments. In particular, it is quite close to U(5) limit, $R_4 = 0$, and SU(3) limit, $R_4 = \frac{10}{7}$ at $N = 86$ and 92, respectively. For $N = 88$ and 90 nuclei, similarly to R_2 and R_3, the present R_4 values suggest a rather rotational feature, compared with the experimental data.

E. Ground-state energies

Now we turn to the description of ground-state energies. We start with the Hamiltonian $\hat{H}_{\rm tot}$ of Eq. (2), taking into account the term E_0. Here E_0 is constant for an individual nucleus and its value is determined so that the minimum of $\langle \hat{H}_{\rm tot} \rangle$ agrees with the total energy of the mean-field ground state, which is denoted by $E_{\rm MF}$, namely

$$E_0 = E_{\rm MF} - \langle \hat{H}_{\rm IBM} \rangle_{\rm min}, \tag{15}$$

where $\langle \hat{H}_{\rm IBM} \rangle_{\rm min}$ stands for the minimum of $\langle \hat{H}_{\rm IBM} \rangle$ in Eq. (8). $E_{\rm MF}$ is the energy of the mean-field intrinsic state. By denoting the ground-state eigenvalue of $\hat{H}_{\rm IBM}$ in Eq. (3) as $E_{\rm IBM}$, the total energy of the IBM system, denoted by $E_{\rm tot}$, is written as

$$E_{\rm tot} = E_0 + E_{\rm IBM}. \tag{16}$$

Namely $E_{\rm tot}$ is nothing but the energy eigenvalue of $\hat{H}_{\rm tot}$ in Eq. (2) for the ground state in the laboratory system, which should be compared with the experiment.

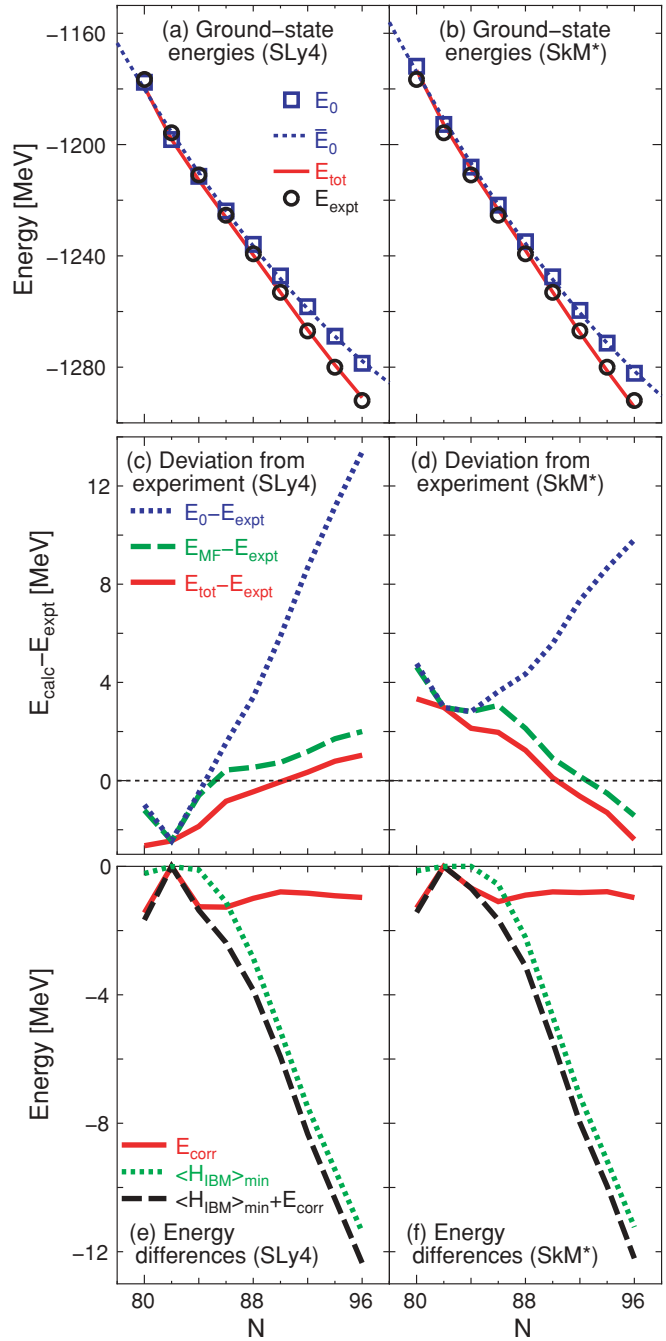

FIG. 8. (Color online) Ground-state energies for Sm isotopes as functions of N, studied with Skyrme SLy4 (left) and SkM* (right) forces. (a and b) E_0, $\bar{E}_0$ [defined in Eq. (17)], $E_{\rm tot}$ and experimental binding energy. (c and d) Deviations of the calculated ground-state energies from experiment. (e and f) $\langle \hat{H}_{\rm IBM} \rangle_{\rm min}$ (contribution from deformation) and $E_{\rm corr}$ (correlation energy) and their sum.

Figures 8(a) and 8(b) show the evolution of E_0, $E_{\rm tot}$, and experimental binding energy $E_{\rm expt}$ as functions of N for Sm isotopes, calculated with the Skyrme SLy4 and SkM* interactions, respectively. The boson number is taken to be $n_\nu = (N - 82)/2$ for $N > 82$, while $n_\nu = (82 - N)/2$ for $N < 82$.

It may be of interest to see n_ν dependencies of E_0 from a simple perspective. E_0 can be approximated, for simplicity, by a polynomial

$$\bar{E}_0 = c_0 + c_1 n_\nu + c_2 n_\nu (n_\nu - 1). \quad (17)$$

Here c_0 represents the contribution from the inert core and c_1 corresponds to the energy needed to remove one neutron boson in a mean potential. The coefficients c_i's are common for all Sm isotopes in $N = 80$–96. We obtain the coefficients in MeV as $c_0 = -1195.510$ (-1190.781), $c_1 = -15.073$ (-16.393), and $c_2 = 0.476$ (0.494) for SLy4 (SkM*) case by a χ-square fit to E_0. The present value of $c_1/2$ is approximately equal to 8 MeV, which is consistent with the empirical value of one-neutron or one-proton separation energy. The fitted functions $\bar{E}_0$'s are shown also in Figs. 8(a) and 8(b) by dotted curves.

In the following, we use the original definition of E_0 shown in Eq. (15). Figures 8(a) and 8(b) illustrate that the experimental binding energies can be reproduced to a good extent only by E_0 in the vicinity of the closed shell $N = 82$, but deviations from experiments become notable for larger N. $E_{\rm tot}$ reproduces the trend of the experimental values quite nicely, including those far away from the shell closure.

$E_{\rm MF}$ is not plotted in Figs. 8(a) and 8(b), since it cannot be distinguished from $E_{\rm tot}$ in the energy scale there. We then perform more precise analyses. In Figs. 8(c) and 8(d), the deviations of the calculated energies E_0, $E_{\rm MF}$, and $E_{\rm tot}$ from the experimental data are depicted as functions of N. The deviations of $E_{\rm MF}$ and $E_{\rm tot}$ are much smaller than that of E_0, particularly for open-shell nuclei, while the calculated results show weak dependence on the Skyrme parameters.

What is of particular importance in Figs. 8(c) and 8(d) is that, while $E_{\rm MF}$ has a kink at the closed shell $N = 82$, $E_{\rm tot}$ evolves smoothly as a function of N even at $N = 82$ and becomes closer to the experimental trend. For both SLy4 and SkM* cases, $E_{\rm tot}$ is lower than $E_{\rm MF}$ all the way by approximately 1 MeV, and this energy difference is largest from nearly spherical to transitional regions, in which the quantum fluctuation effect seems to be most enhanced. In the following, we refer to the energy difference as the *correlation energy* $E_{\rm corr}$, which is written as

$$\begin{aligned} E_{\rm corr} &\equiv E_{\rm tot} - E_{\rm MF} \\ &= E_{\rm tot} - (E_0 + \langle \hat{H}_{\rm IBM} \rangle_{\rm min}). \end{aligned} \quad (18)$$

Here $E_{\rm corr}$ is the difference between the IBM ground-state energy in the laboratory frame and the energy expectation value in the mean field and represents quantum-mechanical contributions in the IBM. The quantity $\langle \hat{H}_{\rm IBM} \rangle_{\rm min}$ can be interpreted as the deformation contribution to the ground-state energy.

We show in Figs. 8(e) and 8(f) the correlation energy $E_{\rm corr}$, $\langle \hat{H}_{\rm IBM} \rangle_{\rm min}$ and their sum, which turns out to be $E_{\rm IBM}$, as functions of N. From around the closed shell $N = 82$ to the transitional region ($N = 88$ or 90), the correlation effect appears to be enhanced in comparison to the deformation contribution $\langle \hat{H}_{\rm IBM} \rangle_{\rm min}$, while $E_{\rm corr}$ becomes somewhat smaller and remains constant all the way from the transitional region toward the middle of the major shell. $\langle \hat{H}_{\rm IBM} \rangle_{\rm min}$ increases as a function of N and accounts for the most part (more than 90%) of $E_{\rm IBM}$ for $N \geqslant 92$, which is obtained by the diagonalization of $\hat{H}_{\rm IBM}$. In other words, for the strong deformation the mean-field model can give, to a certain extent, a reasonable description of the experimental binding energy.

The two-neutron separation energy for IBM (denoted by S_{2n}) can be calculated as a function of n_ν with n_π being fixed:

$$S_{2n}(n_\nu) = -E_{\rm tot}(n_\nu + 1) + E_{\rm tot}(n_\nu). \quad (19)$$

Note that in case the neutrons surpass half of a major shell, where the number of the neutron bosons are counted as that of pairs of neutron holes from the upper end of the major shell, one has to replace S_{2n} of Eq. (19) with its minus. Similarly, the two-neutron separation energy for the mean field (denoted by $S_{2n}^{\rm MF}$) is written as a function of N with fixed Z:

$$S_{2n}^{\rm MF}(N) = -E_{\rm MF}(N + 2) + E_{\rm MF}(N). \quad (20)$$

We show in Fig. 9 the two-neutron separation energies as functions of N calculated with Skyrme SLy4 and SkM* forces. Note that the IBM separation energy S_{2n} is depicted as a function of N, not that of $n_\nu [= (N - 82)/2]$. Both Skyrme forces give similar systematics to the experiments, including the shell gap at $N = 82$ and the plateau from $N = 88$ to 92 which reflects the first-order phase transition from spherical to deformed shapes [45]. Some notable improvement by the inclusion of the correlation effect can be found around the shell closure $N = 82$. Indeed, while $S_{2n}^{\rm MF}$ with SLy4 deviates considerably from the experiment at $N = 84$, S_{2n} appears to be much more consistent with the experiment. This is closely associated with the finding in Figs. 8(c) and 8(d) that the kink which appears around the closed shell $N = 82$ at the mean-field level is eliminated by the inclusion of the correlation energy.

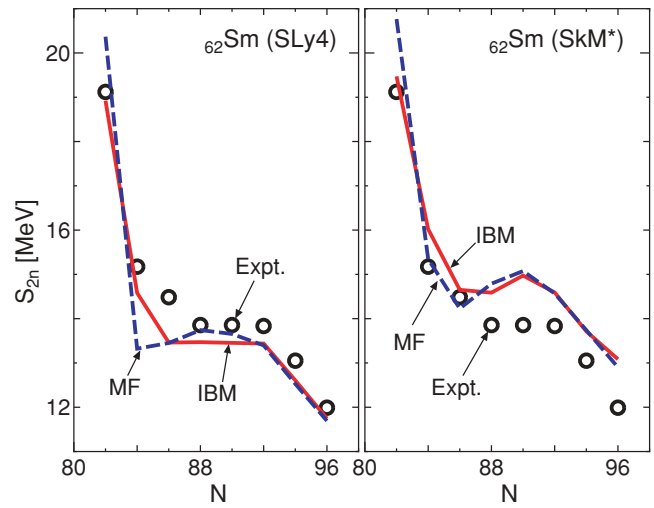

FIG. 9. (Color online) Two-neutron separation energies for Sm isotopes for $N = 82$–96, studies with SLy4 (left panel) and SkM* (right panel) forces. Experimental data are taken from Ref. [56]. Note that the IBM results are depicted as functions of N, instead of n_ν.

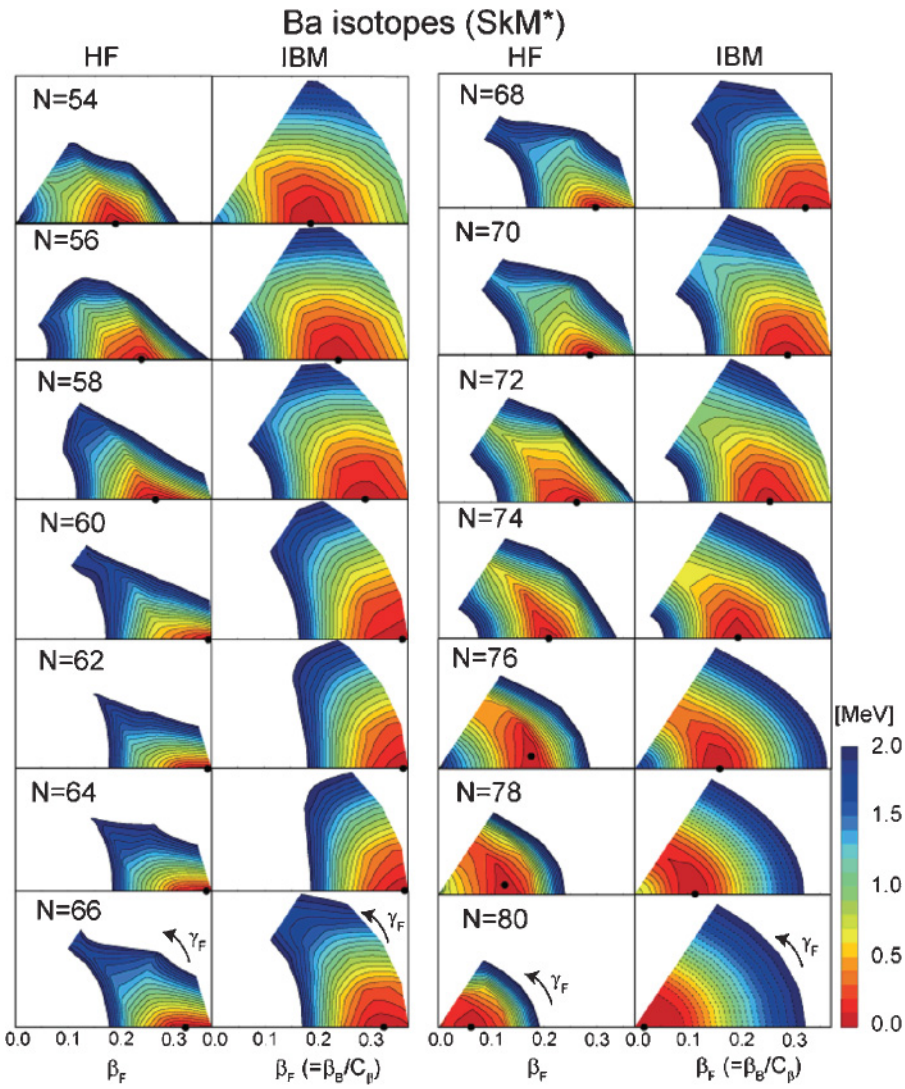

FIG. 10. (Color online) Same as Fig. 2 but for Ba isotopes.

IV. APPLICATIONS

In the following sections, we further apply the present method to Ba, Xe, Ru, and Pd isotopes in the $N = 50$–82 major shell, and to exotic W and Os isotopes beyond the $N = 126$ shell closure, for which no available data exists. The Skyrme SkM* force is used.

A. Ba and Xe isotopes

1. The PES's

Figure 10 shows the comparisons of PES's for Ba isotopes. The HF PES for $N = 54$ indicates a weakly deformed shape with $\beta_{\min} \sim 0.20$.

Away from the closed shells to the open-shell region, the HF PES becomes sharper, particularly for the β direction. Accordingly, $\beta_{\min}$ shifts away from the origin. Somewhat sharp prolate minima can be found from around $N = 56$ to 74, beyond which the HF PES becomes flat in both β and γ directions. This reflects the transition from (prolate) deformed to γ-unstable shapes. The HF PES suggests a nearly spherical shape with a small $\beta_{\min}$ value near the magic number $N = 82$. These transitions of the HF PES are reproduced well by the IBM PES.

The PES's for $N = 76$ and 78 Ba nuclei have large flat areas compared with other Ba nuclei. In the present case, the PES of ^{134}Ba ($N = 78$) is flatter than that of ^{132}Ba ($N = 76$): ^{134}Ba seems to be close to E(5) critical-point symmetry [57], while ^{132}Ba is closer to the O(6) limit of IBM. Indeed, while the $R_{4/2}$ value of the E(5) model is 2.19, the experimental value for ^{134}Ba is $R_{4/2} = 2.31$, which agrees better with the calculated result, 2.50.

We show in Fig. 11 the PES's for Xe isotopes, which exhibit similar systematics to, but are softer and less deformed than, Ba isotopes. The HF PES tends to show a sharp prolate minimum for the open-shell nuclei and becomes flat for $N = 76$ and 78. $N = 80$ nucleus is nearly spherical, which is slightly deformed. The IBM PES's reproduce all these transitions well.

2. Derived IBM parameters

We show in Fig. 12 the evolution of the derived IBM parameters with N for Ba and Xe isotopes, both of which

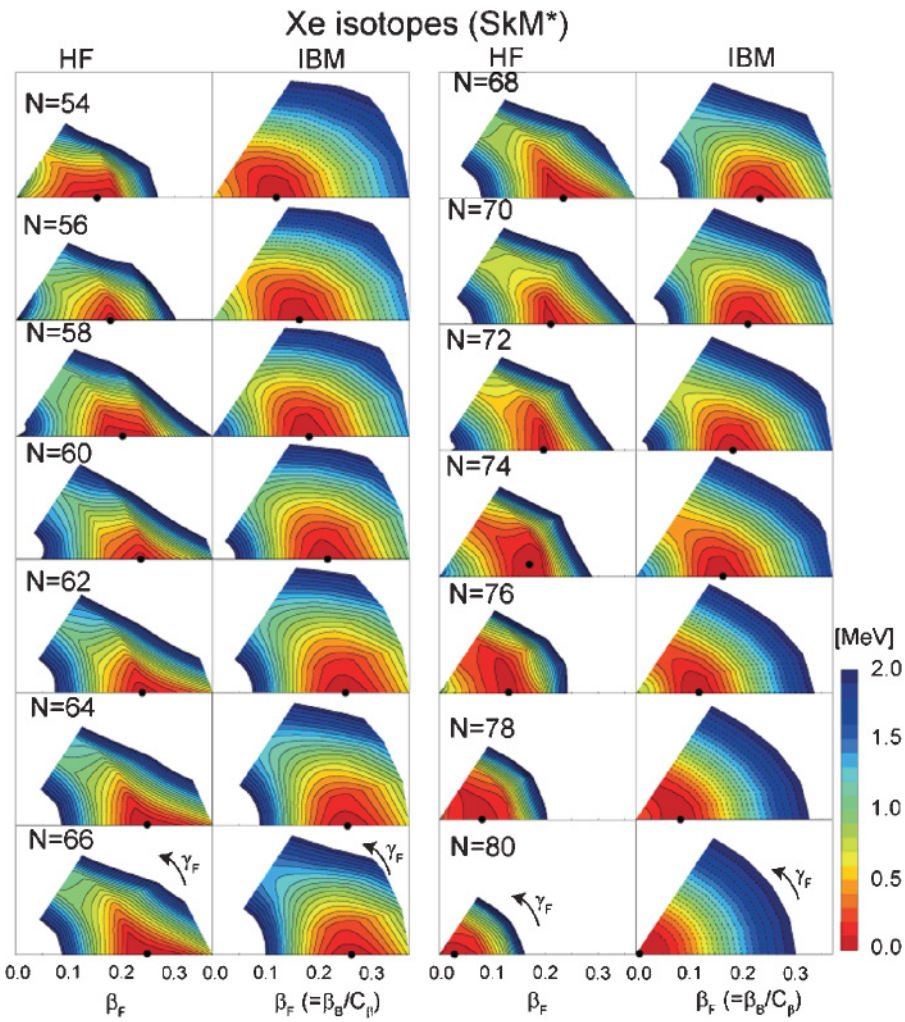

FIG. 11. (Color online) Same as Fig. 2 but for Xe isotopes.

show similar tendencies. While χ_ν increases with N, the quantity $\chi_\pi + \chi_\nu$ is negative all the way and becomes almost zero for $N \geqslant 76$, where the γ softness appears in the PES. χ_π is kept constant as $\chi_\pi = -0.500$ and -0.600 for Ba and Xe isotopes, respectively. ϵ, κ, and C_β are maximal around the middle of the major shell at which the PES shows the largest deformation. ϵ and κ for Xe isotopes are generally larger than those for Ba isotopes. The overall behaviors of the derived parameters in Fig. 12 are consistent with existing phenomenological studies [18], while the magnitude of κ in the present case is much larger.

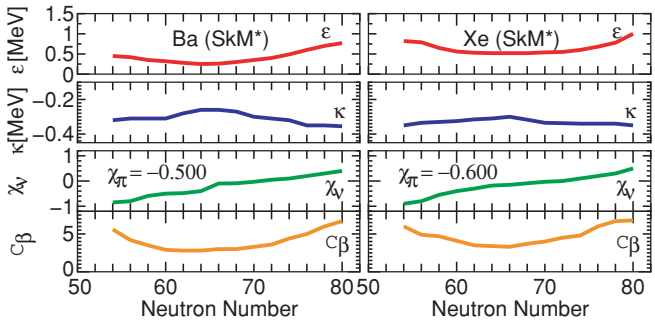

FIG. 12. (Color online) Evolution of the derived IBM parameters for Ba and Xe isotopes with N. χ_π is kept constant as $\chi_\pi = -0.500$ and -0.600 for Ba and Xe isotopes, respectively.

3. *Spectra*

We show in the left panel of Fig. 13 the low-lying spectra for Ba isotopes as functions of N. The calculated yrast levels are particularly in good agreement with the experimental ones. From $N = 54$ to 58, the present calculation suggests that the side-band levels, 0_2^+ and 2_2^+, deviate from 4_1^+ level, exhibiting the transition from the nearly spherical to deformed shapes. When approaching the middle of the major shell, the calculated yrast levels decrease with N consistently with the experimental data, while the present 0_2^+ level shows an opposite dependence on N to the experiments. In the open-shell region, the calculated levels resembles rotational spectra. Indeed the $R_{4/2}$ values of $N = 62$, 64, and 66 in the present calculation are 3.23, 3.23, and 3.14, respectively, being close to the SU(3) limit ($R_{4/2} = 3.33$), while those of the experiments are 2.86, 2.92, and 2.90, respectively. There are some deviations of the side-band levels for lighter Ba isotopes. In the present study, however, one cannot always obtain much information about

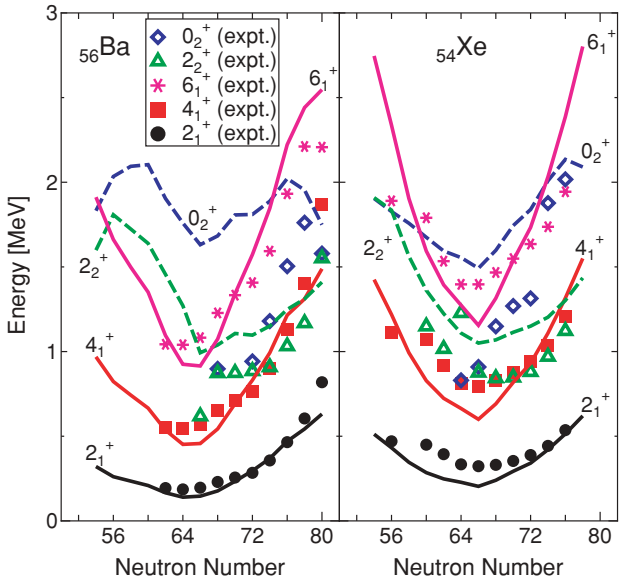

FIG. 13. (Color online) Level evolution in Ba and Xe isotopes. Symbols and curves stand for the calculated results and the experimental data [47], respectively, as indicated in the figure.

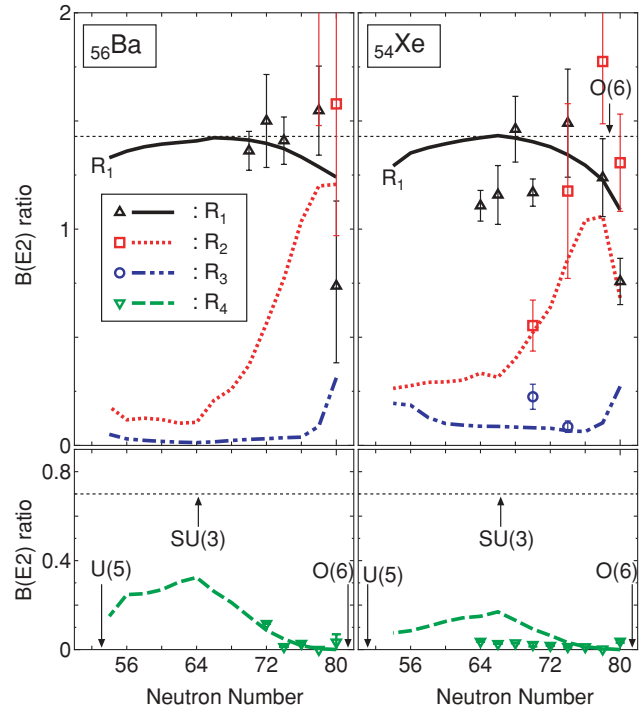

FIG. 14. (Color online) B(E2) ratios for Ba (left panel) and Xe (right panel) isotopes as functions of N for $54 \leqslant N \leqslant 80$. Curves stand for the calculated B(E2) ratios R_1-R_4, which are defined in Eq. (14). Experimental data (represented by the symbols) are taken from Refs. [59].

the side-band structures only by referring to the HF PES. The improvement of the side-band levels should be an interesting future subject.

Approaching the shell closure $N = 82$, each level goes up and one sees the level structure of γ-unstable nuclei at $N = 76$ and 78 similarly to the experimental data. In fact, the 4_1^+ state is pushed up to be relatively close to the 2_2^+ and 0_2^+ states. This is a characteristic feature of the γ-unstable nuclei. At $N = 80$, $4_1^+, 0_2^+$, and 2_2^+ states lie close to each other, which is characteristic of the spherical vibrator. In addition, the calculated $R_{4/2}$ values for $N = 76$, 78, and 80 Ba nuclei are 2.58, 2.50, and 2.36, respectively, where the first two are close to the O(6) limit ($R_{4/2} = 2.50$) and the last one U(5) limit ($R_{4/2} = 2.00$). Experimental $R_{4/2}$ values for $N = 76$, 78, and 80 Ba nuclei are 2.58, 2.31, and 2.28, respectively, which are fairly close to the present calculations.

The right panel of Fig. 13 shows the excitation spectra for Xe isotopes. The experimental tendencies are reproduced by the present calculations fairly well. Similarly to the HF PES's, the calculated excitation spectra for lighter Xe nuclei are somewhat more rotational-like, compared with the experiments. The properties of γ-unstable structures for $N = 76$ and 78 nuclei are well reproduced. Indeed, the calculated and the experimental $R_{4/2}$ values for $N = 76$ (78) Xe nucleus are 2.48 (2.54) and 2.25 (2.94), respectively, which are fairly consistent.

The HF PES's for ^{132,134}Ba and ^{128}Xe have triaxial minima, while the IBM PES's do not reproduce them. In the present study, a triaxial minimum in the HF PES is approximated by a flat IBM PES by putting $\chi_\pi + \chi_\nu \simeq 0$ in Eq. (8). Even under such simplification, the calculated levels for γ-unstable nuclei are in good agreement with the data. This may be the similarity of the level pattern between the γ softness and the rigid triaxiality, which has been discussed in Ref. [58].

4. *B(E2) ratios*

We show in Fig. 14 the B(E2) ratios for Ba and Xe isotopes as functions of N. The calculated R_1 value does not show a strong dependence on N for both Ba and Xe isotopes, while it increases toward the middle of the major shell, being in the vicinity of the O(6) limit, $R_1 = \frac{10}{7}$. R_2 changes rather significantly. For $N = 54$–64 the calculated R_2 value is in the vicinity of the SU(3) limit, $R_2 = 0$, and becomes larger toward the shell closure $N = 82$, taking the maximal value close to O(6) limit, $R_2 = \frac{10}{7}$ at around $N = 76$ or 78. In the open-shell region, the present value of R_2 for Ba isotopes is closer to zero than Xe isotopes, where the former indicates more rotational feature of SU(3) limit than the latter. For Xe isotopes, the calculated R_2 shows a similar trend to the available data. At $N = 78$, the present R_2 value for Ba isotopes is closer to the O(6) limit than the Xe isotopes. The R_3 value does not change too much and is close to zero for open-shell nuclei. Its sharp increase for $N \geqslant 78$ may indicate the transition from deformed to γ soft or to a nearly spherical shape. R_3 of Ba isotopes is smaller than that of Xe isotopes all the way, which suggests stronger deformation. R_4 increases monotonically from around the shell closures to the middle of the major shell at which it becomes maximal. R_4 of Ba isotopes is generally larger than that of Xe isotopes. The calculated values for both isotopes are fairly consistent with the experiment for $N = 72$–80.

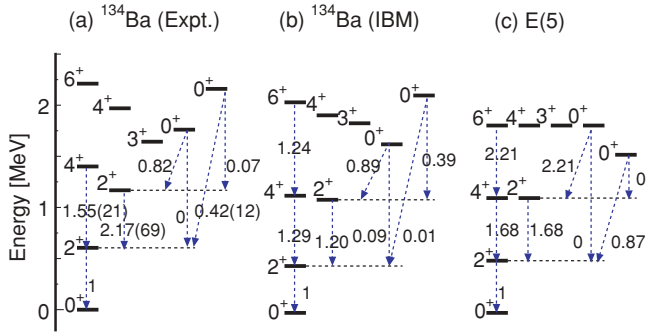

FIG. 15. (Color online) Level schemes and B(E2) ratios for (a) the experimental [47,59] and (b) the calculated (IBM from SkM*) results for ^{134}Ba, and (c) the E(5) model. The 2_1^+ energy of the E(5) model is set equal to the experimental one, $E(2_1^+) = 605$ keV.

5. Comparison with E(5) model

We discuss a particular nucleus, ^{134}Ba, which has been recognized as a manifestation of E(5) symmetry [60]. Figure 15 shows detailed level schemes of (a) the experimental data [47,59], (b) the calculated result for ^{134}Ba, and (c) the E(5) model. Note that the 2_1^+ energy of E(5) is adjusted to 605 keV, which is the experimental 2_1^+ energy for ^{134}Ba.

In the E(5) model, a schematic potential is assumed in addition to the infinite-N limit [57]. This is not the case with actual nuclei, which results in the deviations of the calculated and the experimental excitation levels from E(5) ones as seen from Fig. 15. Indeed, the 6_1^+, 4_2^+, 3_1^+, and 0_3^+ levels are degenerate in the E(5) model, while the overall patterns of the experimental and the calculated level schemes for ^{134}Ba seem to resemble O(6) rather than E(5).

The present values of the B(E2) ratios for $4_1^+ \to 2_1^+$ and $2_2^+ \to 2_1^+$ transitions are smaller than the experimental data, while the 0_2^+ level and the B(E2) ratios for $0_2^+ \to 2_1^+$ and $0_2^+ \to 2_2^+$ transitions agree with the experiments nicely. From the trends of $0_2^+ \to 2_1^+$ and $0_2^+ \to 2_2^+$ transitions, the 0_2^+ state in the present calculation may be related to the third 0^+ state of the E(5) level scheme in Fig. 15(c), which is, using ξ and τ quantum numbers of the E(5) model [57], the $0_{\xi=1,\tau=3}$ state.

B. Ru and Pd isotopes

1. PES

We show in Fig. 16 the PES's for Ru isotopes for $N = 54$–80. The shape of the PES changes with N moderately compared with the Ba and Xe isotopes. For $N = 54$–62, the HF PES suggests a nearly spherical structure, which is slightly prolate deformed. The flat area in the β-γ plane becomes larger from $N = 62$ to 64 significantly, which suggests the transition from nearly spherical to γ-unstable shapes. The HF PES of Ru isotopes exhibits a weak triaxial deformation for $N = 64$–70, which is described by the flat IBM PES with $\chi_\pi + \chi_\nu \sim 0$. As seen in Fig. 16, the HF PES for $N = 64$–70 is complicated

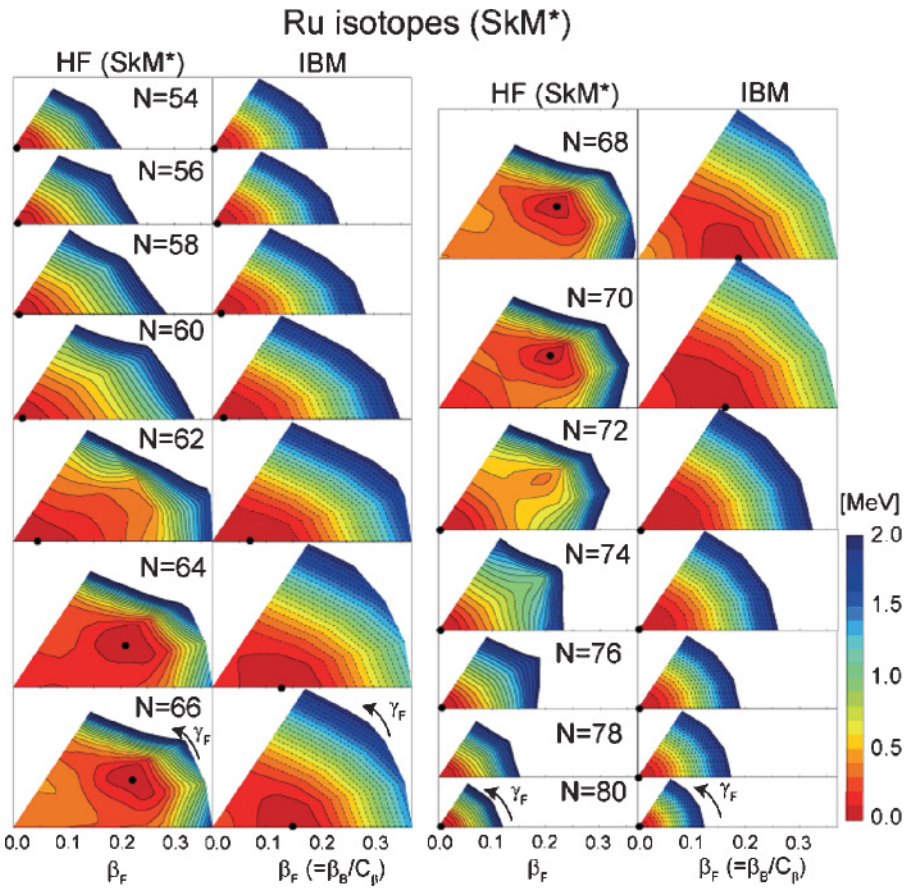

FIG. 16. (Color online) Same as Fig. 2 but for Ru isotopes.

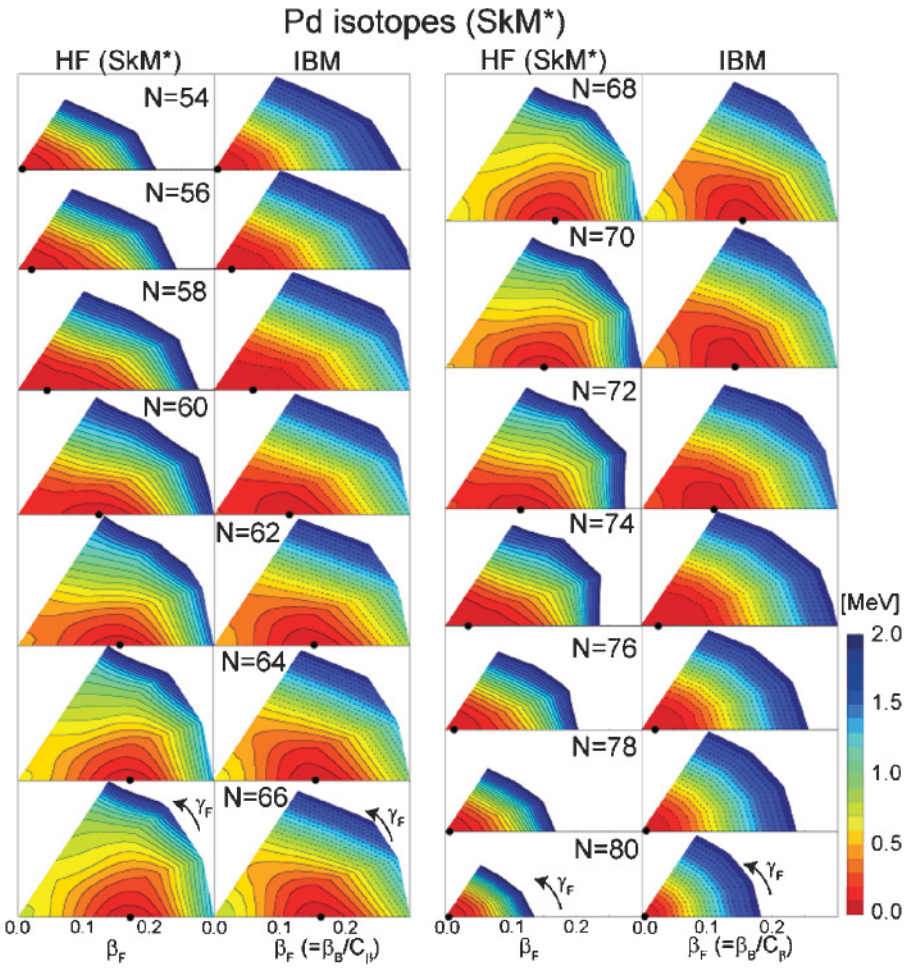

FIG. 17. (Color online) Same as Fig. 2 but for Pd isotopes.

so that it behaves like an infinite wall. This cannot be reproduced by the IBM PES of Eq. (8) and is far beyond the limit of the present PES fit.

The PES's for Pd isotopes are depicted in Fig. 17. The HF PES exhibits spherical structures in the vicinity of the shell closures $N = 50$ and 82 and shows a shallow prolate minimum for the open-shell region, without any notable change of the degree of deformation. This flat and weakly prolate deformed structure can be seen in a wide range of the neutron number, $N = 60$–72. These trends of the HF PES's are nicely reproduced by the IBM PES's. Unlike some Ru isotopes, the HF PES for Pd isotopes is rather simple overall to be reproduced well by the IBM PES.

2. *Derived IBM parameters*

We show in Fig. 18 the evolution of the derived IBM parameters. The overall tendencies of ϵ, κ, and C_β are common for both Ru and Pd isotopes, although there are quantitative differences to a certain extent. χ_π is kept constant as $\chi_\pi = -0.500$ and -0.600 for Ru and Pd isotopes, respectively. For Ru isotopes, χ_ν becomes larger with N but slightly decreases for $N \geqslant 74$, while, for Pd isotopes, it increases from $N = 54$ to 66, around which it becomes constant and begins to decrease from $N = 70$. For $N \geqslant 66$, the magnitude of $\chi_\pi + \chi_\nu$ is slightly larger with a negative sign in the Pd isotopes than in the Ru isotopes, reflecting that the PES of the former is somewhat steeper in the γ direction than that of the latter, while both are similarly flat in β direction. The variation of C_β reflects the gradual change of $\beta_{\min}$. In the earlier phenomenological work [19], χ_ν increases monotonically and χ_π is opposite in sign to the present parameter values for both Ru and Pd isotopes. Other parameters in [19] are generally consistent with the present ones.

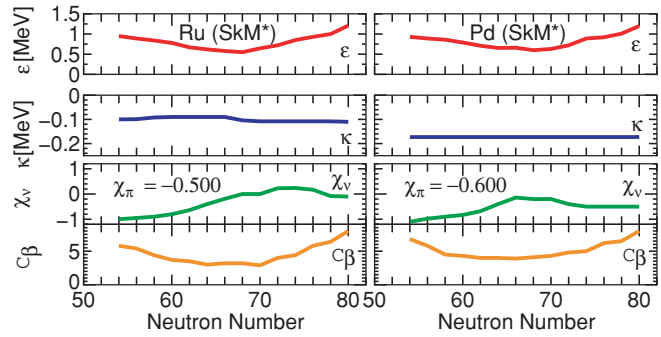

FIG. 18. (Color online) Evolution of the IBM parameters for Ru and Pd isotopes studied with SkM* force. χ_π is kept constant as -0.500 and -0.600 for Ru and Pd, respectively.

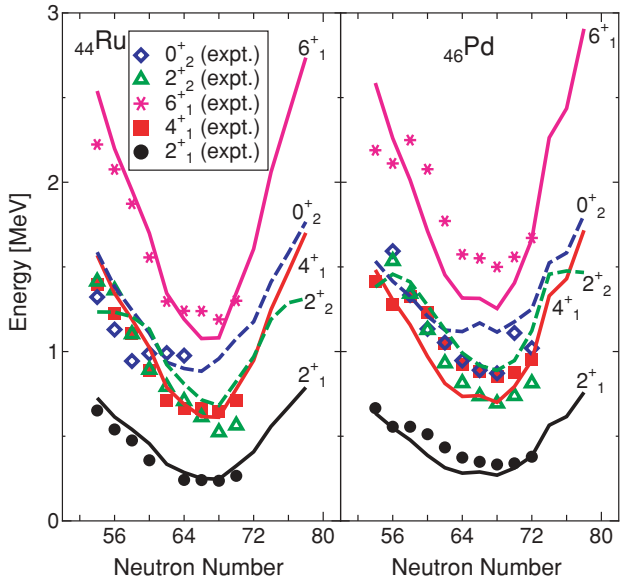

FIG. 19. (Color online) Same as Fig. 13 but for Ru and Pd isotopes.

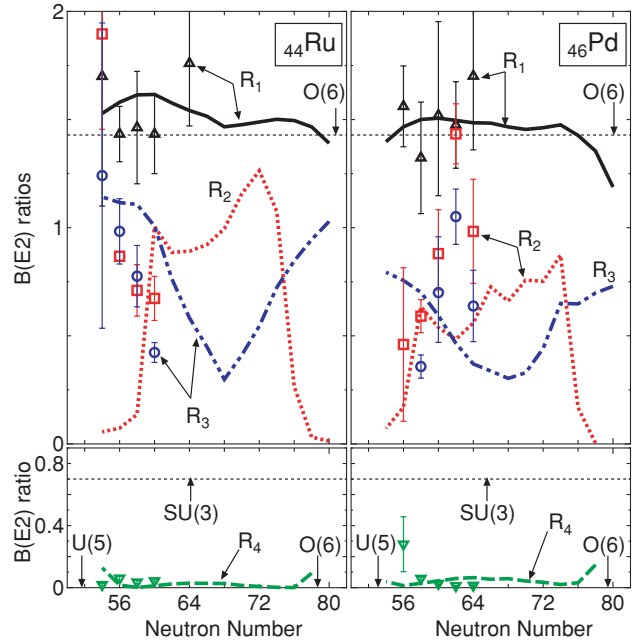

FIG. 20. (Color online) Same as Fig. 14 but for Ru and Pd isotopes. Data are taken from Refs. [64].

3. Spectra

Figure 19 exhibits the evolution of low-lying spectra as functions of N for Ru and Pd isotopes.

For both Ru and Pd isotopes, the calculated spectra in the vicinity of the shell closure $N = 50$ look like those of a spherical vibrator, where 4_1^+, 0_2^+, and 2_2^+ form the triplet, which is characteristic of the U(5) limit. This level structure is commonly found to continue from $N = 54$ to around $N = 62$. For $N = 64$–70, each calculated level comes down with the increase of N to show as a whole the O(6)-like level scheme. Of the triplet 4_1^+, 0_2^+, and 2_2^+, only the 0_2^+ state is not lowered and remains close to the 6_1^+ state. This is characteristic of the γ-soft O(6) nuclei. Thus $N = 62$ nuclei are supposed to be critical points of the U(5)-O(6) transition. For the Ru isotopes, the behavior of the calculated 0_2^+ level is in good agreement with experimental one, while the experimental 4_1^+, 0_2^+, and 2_2^+ levels remain degenerated all the way, being characteristic of the vibrational level pattern. However, the calculated 0_2^+ energy of Pd isotopes is somewhat larger (or more rotational-like) than the experiment.

Similarly to Ba and Xe isotopes in the $A \sim 130$ region, shallow triaxial minima in the HF PES's for $N = 64$–70 Ru nuclei are approximated by flat IBM PES's, which results in the good agreement of the excitation spectra. For the precise description of the side-band levels, however, some minor contribution which produces a triaxial minimum may need to be added to the boson Hamiltonian, such as the three-body or cubic term [61–63]. The role of the cubic term has been discussed in the context of the odd-even staggering in the quasi-γ band of Ru isotopes [62,63]. In the future it should be interesting to study the microscopic origin of the cubic term.

At $N = 72$, the calculated 4_1^+, 0_2^+, and 2_2^+ levels form the triplet consistently with the experimental data, where the overall level pattern resembles the vibrational level structure. The present calculation predicts this level pattern continues for $N \geqslant 74$. In each isotopic chain there seems to be another critical point of the O(6)-U(5) transition around $N = 70$.

4. B(E2) ratios

In Fig. 20, we show the evolution of the B(E2) ratios R_1-R_4 [defined in Eq. (14)] for Ru and Pd isotopes as functions of N. The calculated R_1 is close to the O(6) limit, $R_1 = \frac{10}{7}$, being consistent with the experiments. R_2 seems to be more sensitive to N, reflecting the structural change. In Ru isotopes, R_2 increases sharply from $N = 54$ to 60 and changes much less for $N = 60$–66, reflecting the sustained γ instability. From there it goes up again and has a maximum value at $N = 72$. The experimental data show the opposite dependence on N, whereas they have large error bars. A sudden drop from around $N = 72$ can be seen in the calculated result for the Ru isotopes, approaching zero around $N = 78$. For the Pd isotopes, R_2 has a similar, but somewhat weaker dependence on N compared with the Ru isotopes, and suggests smaller values in the open-shell region. The behavior of R_3 is rather simple in the present study. For both Ru and Pd isotopes, it decreases away from the closed shells to the open-shell region consistently with the experimental data. The calculated R_4 values both for Ru and Pd isotopes are close to zero [U(5) and O(6) limits] all the way, similarly to the experimental data.

C. W and Os isotopes

Having done the reasonable comparisons with experiments in various situations, we describe unexplored nuclei, W and Os isotopes with $N > 126$. They are chosen because no systematic theoretical work has been done on these unexplored nuclei. Note that the PES fit for W isotopes in this article is the

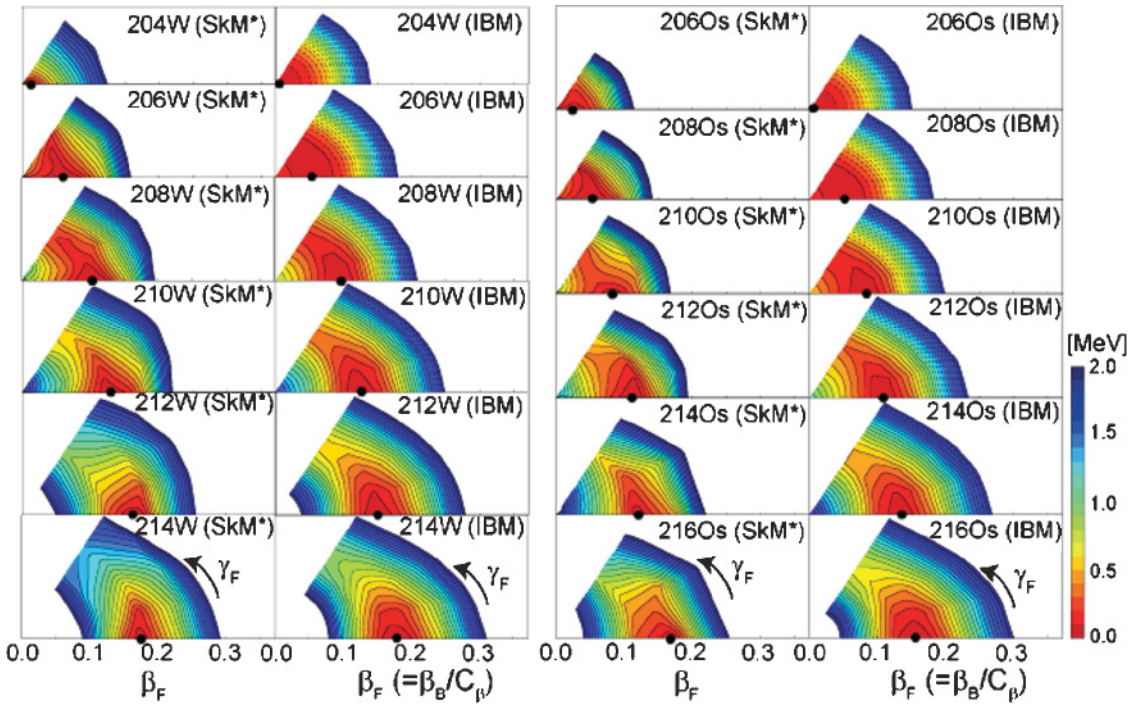

FIG. 21. (Color online) Same as Fig. 2 but for W and Os isotopes.

refinement of our previous calculation [32], but the qualitative feature remains the same.

1. The PES's and the derived IBM parameters

The HF and IBM PES's for W and Os isotopes are compared in Fig. 21 for $N = 130$–140. The HF PES's for $N = 130$ nuclei, ^{204}W and ^{206}Os, have the minima at $\beta \sim 0$, being similar to the harmonic oscillator potential characteristic of the vibrational or U(5) limit. The corresponding IBM PES's generally look somewhat flatter, but the overall patterns are almost the same as the HF ones. In both W and Os isotopes, the location of the energy minimum shifts gradually to $\beta \neq 0$ with N and the PES becomes steeper in the γ direction, while the flat area becomes larger. This large flat area, characteristic of E(5) symmetry, continues from $N = 132$ to 136, while the change of the PES for Os isotopes looks moderate in comparison to the W isotopes. For the $N = 134$ nuclei, ^{208}W and ^{210}Os, for instance, which are located on the way to the shape transition, the PES's exhibit a typical O(6)-E(5) structure similarly to the ^{132,134}Ba nuclei. Indeed, the predicted $R_{4/2}$ values for ^{208}W and ^{210}Os are 2.49 and 2.45, respectively, both of which are close to the E(5) value (=2.19) and also with the experimental $R_{4/2}$ value of ^{134}Ba (=2.31). For $N \geqslant 140$, the HF PES suggests stronger deformation.

We show in Fig. 22 the evolution of the derived IBM parameters for W and Os isotopes. Of particular interest is that χ_π and χ_ν have opposite signs with sizable magnitudes for $N \geqslant 130$. In the IBM-2, this is the origin of the O(6)-E(5) pattern [5,6,10]. Each parameter does not change too much with N since there is no drastic change of the PES.

2. Spectra and B(E2) ratios

In Fig. 23 the level evolution for W and Os isotopes is shown. It is of considerable interest that the magnitude of deformation, represented by the decrease of 2_1^+ level, becomes larger with N, while the γ-unstable E(5)-O(6) level pattern is maintained all the way. Such sustained E(5)-O(6) level structure has never been seen in stable nuclei and may become one of the characteristic features of exotic nuclei with considerable neutron excess. While we assume in the present study that the proton and the neutron systems move in phase, these restrictions could be relaxed. The mechanism which causes such an unexpectedly large region of the E(5) pattern would be also studied in the future. For $N \geqslant 136$ or 138, the calculated 4_1^+ level continues to decrease with N, while the 2_2^+ state gradually increases. This indicates the structural

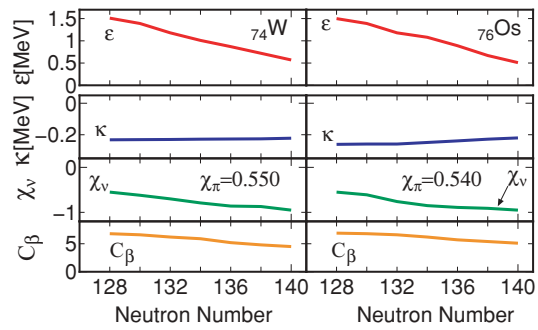

FIG. 22. (Color online) Evolution of the IBM parameters with N for W and Os isotopes. χ_π is kept constant as $\chi_\pi = 0.550$ and 0.540 for W and Os isotopes, respectively.

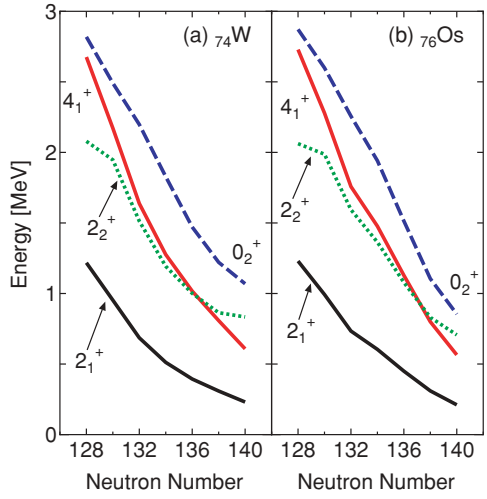

FIG. 23. (Color online) Calculated excitation levels of (a) W and (b) Os isotopes as functions of N.

evolution from γ-soft to axially symmetric deformed nuclei. While these tendencies can be found commonly in W and Os isotopes, the transition in Os isotopes occurs moderately compared with W isotopes.

We show in Fig. 24 the predicted B(E2) ratios. While R_1 is almost constant, being close to the O(6) limit ($=\frac{10}{7}$), R_2 becomes larger with N and becomes maximal at around $N = 132$ for W isotopes and around $N = 132$ or 134 for Os isotopes. The R_2 value looks closer to that of the O(6) limit and that of $E(5)$ model (=1.67) for $N = 132$–136, while for Os isotopes,

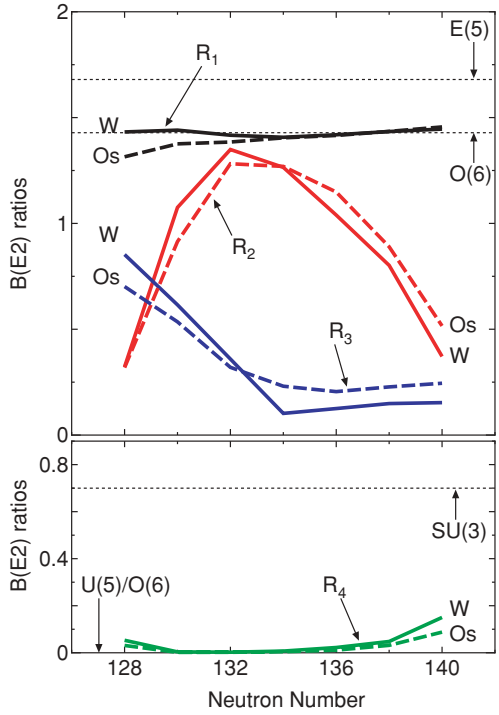

FIG. 24. (Color online) Calculated B(E2) ratios for W (solid curves) and Os (dashed curves) isotopes as functions of N. R_1-R_4 are defined in Eq. (14).

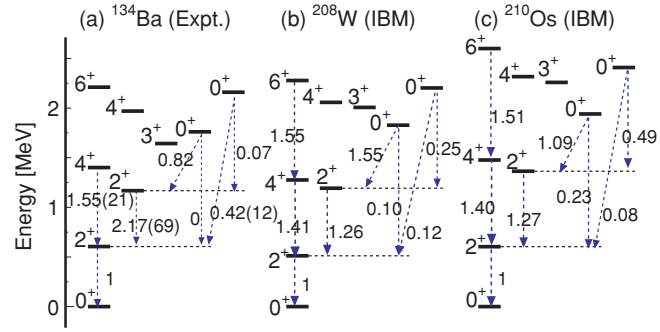

FIG. 25. (Color online) Level schemes and B(E2) ratios. (a) Experimental data for ^{134}Ba [47,59]; calculated results for (b) ^{208}W and (c) ^{210}Os.

R_2 changes with N less significantly than for W isotopes. This moderate change of R_2 may be also a characteristic feature of the sustained γ softness which can be found in the PES and in the excitation spectra. R_3 gradually decreases with N similarly to the Ru isotopes, which suggests structural change. R_4 remains almost zero, being much below the SU(3) limit, $R_4 = \frac{7}{10}$.

3. *Comparison with the E(5) model*

For the sake of completeness, we show in Fig. 25 the detailed level schemes, focusing on the $N = 134$ nuclei, ^{208}W and ^{210}Os, which may be candidates for E(5) critical points. The calculated results of (b) ^{208}W and (c) ^{210}Os are compared with (a) the experimental level scheme for ^{134}Ba nucleus [47,59]. The calculated B(E2) is generally smaller than the E(5) one of Fig. 15(c). For both ^{208}W and ^{210}Os, the calculated B(E2) ratios for the transitions from the yrast to the side-band levels show quite similar trends to the experiments for ^{134}Ba, except for the $0_3^+ \to 2_1^+$ and $0_3^+ \to 2_2^+$ transitions. The calculated B(E2) ratios for $0_2^+ \to 2_2^+$ transition are 1.55 and 1.09 for ^{208}W and for ^{210}Os, respectively, both of which are closer to the E(5) value (=2.17) than the calculated value for ^{134}Ba (=0.89) in Fig. 15(b) and the experimental data for ^{134}Ba (=0.82). Moreover, particularly for ^{208}W, levels of 6_1^+, 4_2^+, 3_1^+, and 0_2^+ states are to a greater extent degenerated than those of ^{134}Ba, which is rather O(6)-like. This may also be an evidence that there exist many examples to exhibit E(5)-like features in the $N > 126$ region.

V. SUMMARY

In summary, we have presented a mean-field based formulation of the IBM for general cases. The mean-field methods and the IBM can help each other to yield levels and wave functions, which cannot be calculated easily by the former with good quantum numbers in the laboratory system. The present approach is based on the assumption that multifermion dynamics of the surface deformations can be simulated in terms of bosons so that the effects of nuclear forces and the Pauli principle are incorporated into the mathematically simpler boson model. While the IBM is a model for collectivity, the shell-model interaction contains many aspects, some of which are enhanced, but others are suppressed for low-lying

collective states. Treating all these aspects precisely with a usual truncation like seniority may not be so easy. Standard Skyrme mean-field models are useful for bulk and surface properties with good calibration to experiment and are suitable to start with.

By applying the wavelet analysis, we have demonstrated that the physically relevant IBM parameters can be derived unambiguously. Three kinds of the wavelet functions have been considered in the present work, and we would like to emphasize that any of these wavelets turns out to give almost the same parameters as those without using wavelets (w/o-wavelet fit). The resultant excitation spectra are also consistent with the experimental data to almost the same extent as the w/o-wavelet calculations.

We have reproduced the transition from spherical to deformed shapes in Sm isotopes successfully. For strongly deformed Sm isotopes, however, there arises the problem that the calculated yrast levels become systematically higher than the experiments, requiring us to introduce an additional term such as $L \cdot L$ term of the boson Hamiltonian. We point out once again that a general IBM-2 Hamiltonian may contain some interactions, including the $L \cdot L$ term, which cannot be determined by simply comparing the PES's but make a certain contribution to the excitation spectra. In this article, we have not taken into account such interactions for simplicity. In the future, some response of the nucleonic system, e.g., a rotation of a strongly deformed object, may need to be formulated.

In addition, the present method has been used for evaluating the quantum effect in the ground-state energy, taking Sm isotopes as an example. We have demonstrated that the correlation energy which comes from the quantum-mechanical calculation by the IBM contributes to a good extent to reproducing the tendency of the experimental binding energy.

The present method has been applied to several other isotopic chains in comparison to experiments. For Ba and Xe isotopes, we have shown that the calculated levels and the B(E2) ratios exhibit signs of shape transitions involving γ-unstable, O(6) nuclei. Of particular interest are the spectra of some γ-soft nuclei having shallow triaxial minimum in their HF PES's. We then approximate such triaxiality by a flat IBM PES. Even under this simplification, the calculated yrast levels agree with experiments reasonably well. The precise description of the side-band levels should be an important future subject, while it may be also interesting to construct a more universal Skyrme interaction. In Ru and Pd isotopes, we have reproduced and predicted the transition between spherical and γ-unstable shapes, together with what seem to be the critical points. The calculated spectra are in much better agreement with the experimental ones as compared to the Ba-Xe region, while the PES fits also appear to be fine.

The present approach is also capable of predicting the spectroscopic properties of experimentally unexplored nuclei with $N > 126$, for which no extrapolation has been possible. This may stimulate experimental efforts using rare-isotope beams to produce heavy exotic nuclei.

ACKNOWLEDGMENTS

The authors thank Professors R. F. Casten, A. Gelberg, P.-H. Heenen, and W. Nazarewicz for valuable discussions. The authors are also grateful to Dr. Dee A. Worman for reading the manuscript. This work has been supported in part by Grant-in-Aid for Scientific Research (A) 20244022, by Grant-in-Aid for JSPS Fellows (No. 217368), by the JSPS Core to Core program "International Research Network for Exotic Femto Systems" (EFES), and by the Inoue Foundation for Science.

[1] A. Bohr and B. R. Mottelson, *Nuclear Structure* (Benjamin, New York, 1969 and 1975), Vols. I and II.
[2] P. Ring and P. Schuck, *The Nuclear Many-Body Problem* (Springer, Berlin, 1980).
[3] A. Arima and F. Iachello, Phys. Rev. Lett. **35**, 1069 (1975).
[4] F. Iachello and A. Arima, *The Interacting Boson Model* (Cambridge University Press, Cambridge, 1987).
[5] T. Otsuka, A. Arima, F. Iachello, and I. Talmi, Phys. Lett. B **76**, 139 (1978).
[6] T. Otsuka, A. Arima, and F. Iachello, Nucl. Phys. A **309**, 1 (1978).
[7] A. Arima and F. Iachello, Ann. Phys. (NY) **99**, 253 (1976).
[8] A. Arima and F. Iachello, Ann. Phys. (NY) **111**, 201 (1978).
[9] A. Arima and F. Iachello, Ann. Phys. (NY) **123**, 468 (1979).
[10] T. Otsuka, in *Algebraic Approaches to Nuclear Structure*, edited by R. F. Casten (Harwood, Chur, 1993), p. 195.
[11] T. Mizusaki and T. Otsuka, Prog. Theor. Phys. Suppl. **125**, 97 (1997).
[12] M. Deleze, S. Drissi, J. Kern, P. A. Tercier, J. P. Vorlet, J. Rikovska, T. Otsuka, S. Judge, and A. Williams, Nucl. Phys. A **551**, 269 (1993).
[13] K. Allaart, G. Bonsignori, M. Savoia, and V. Paar, Nucl. Phys A **458**, 412 (1986).
[14] Y. K. Gambhir, P. Ring, and P. Schuck, Phys. Rev. C **25**, 2858 (1982).
[15] O. Scholten, Phys. Rev. C **28**, 1783 (1983).
[16] T. Otsuka, Phys. Lett. B **138**, 1 (1984).
[17] T. Otsuka and N. Yoshinaga, Phys. Lett. B **168**, 1 (1986).
[18] G. Puddu, O. Scholten, and T. Otsuka, Nucl. Phys. A **348**, 109 (1980).
[19] P. Van Isacker and G. Puddu, Nucl. Phys. A **348**, 125 (1980).
[20] U. Kaup and A. Gelberg, Z. Phys. A **293**, 311 (1979).
[21] P. D. Duval and B. R. Barrett, Phys. Rev. C **23**, 492 (1981).
[22] R. Bijker, A. E. L. Dieperink, O. Scholten, and R. Spanhoff, Nucl. Phys. A **344**, 207 (1980).
[23] T. H. R. Skyrme, Nucl. Phys. **9**, 615 (1959).
[24] D. Vautherin and D. M. Brink, Phys. Rev. C **5**, 626 (1972).
[25] M. Bender, P.-H. Heenen, and P.-G. Reinhard, Rev. Mod. Phys. **75**, 121 (2003).
[26] J. Dobaczewski, M. V. Stoitsov, W. Nazarewicz, and P.-G. Reinhard, Phys. Rev. C **76**, 054315 (2007).
[27] M. Bender, P. Bonche, T. Duguet, and P.-H. Heenen, Phys. Rev. C **69**, 064303 (2004).
[28] M. Bender and P.-H. Heenen, Phys. Rev. C **78**, 024309 (2008).
[29] M. Bender, G. F. Bertsch, and P.-H. Heenen, Phys. Rev. C **73**, 034322 (2006).

[30] D. Lacroix, T. Duguet, and M. Bender, Phys. Rev. C **79**, 044318 (2009); M. Bender, T. Duguet, and D. Lacroix, *ibid.* **79**, 044319 (2009); T. Duguet, M. Bender, K. Bennaceur, D. Lacroix, and T. Lesinski, *ibid.* **79**, 044320 (2009).

[31] P. Bonche, J. Dobaczewski, H. Flocard, P.-H. Heenen, and J. Meyer, Nucl. Phys. A **510**, 466 (1990).

[32] K. Nomura, N. Shimizu, and T. Otsuka, Phys. Rev. Lett. **101**, 142501 (2008).

[33] P. Bonche, H. Flocard, and P.-H. Heenen, Comput. Phys. Commun. **171**, 49 (2005).

[34] P. Bonche, H. Flocard, P.-H. Heenen, S. J. Krieger, and M. S. Weiss, Nucl. Phys. A **443**, 39 (1985).

[35] E. Chabanat, P. Bonche, P. Haensel, J. Meyer, and R. Schaeffer, Nucl. Phys. A **635**, 231 (1998).

[36] J. Bartel, Ph. Quentin, M. Brack, C. Guet, and H.-B. Håkansson, Nucl. Phys. A **386**, 79 (1982).

[37] H. J. Lipkin, Ann. Phys. **9**, 272 (1960).

[38] Y. Nogami, Phys. Rev. **134**, B313 (1964).

[39] H. C. Pradhan, Y. Nogami, and J. Law, Nucl. Phys. A **201**, 357 (1973).

[40] A. E. L. Dieperink and O. Scholten, Nucl. Phys. A **346**, 125 (1980).

[41] J. N. Ginocchio and M. Kirson, Nucl. Phys. A **350**, 31 (1980).

[42] A. Bohr and B. R. Mottelson, Phys. Scr. **22**, 468 (1980).

[43] P. Van Isacker and J.-Q. Chen, Phys. Rev. C **24**, 684 (1981).

[44] T. Otsuka and N. Yoshida, JAERI-M Report 85, 1985.

[45] O. Scholten, F. Iachello, and A. Arima, Ann. Phys. (NY) **115**, 325 (1978).

[46] T. Otsuka, Phys. Rev. Lett. **46**, 710 (1981); T. Otsuka and J. N. Ginocchio, *ibid.* **55**, 276 (1985).

[47] Brookhaven National Nuclear Data Center (NNDC) http://www.nndc.bnl.gov/nudat2/index.jsp.

[48] F. Iachello, Phys. Rev. Lett. **87**, 052502 (2001).

[49] R. F. Casten and N. V. Zamfir, Phys. Rev. Lett. **87**, 052503 (2001).

[50] T. Nikšić, D. Vretenar, G. A. Lalazissis, and P. Ring, Phys. Rev. Lett. **99**, 092502 (2007).

[51] For instance, R. R. Rodriguez-Guzman, J. L. Egido, and L. M. Robledo, Phys. Rev. C **69**, 054319 (2004).

[52] G. Kaiser, *A Friendly Guide to Wavelets* (Boston Birkhäuser, 1994).

[53] C. Torrence and G. P. Compo, Bull. Am. Meteorol. Soc. **79**, 61 (1998).

[54] A. Shevchenko *et al.*, Phys. Rev. C **77**, 024302 (2008).

[55] M. R. Bhat, Nucl. Data Sheets **89**, 797 (2000); H. G. Börner, P. Mutti, M. Jentschel, N. V. Zamfir, R. F. Casten, E. A. McCutchan, and R. Krüken, Phys. Rev. C **73**, 034314 (2006); W. D. Kulp, J. L. Wood, J. M. Allmond, J. Eimer, D. Furse, K. S. Krane, J. Loats, P. Schmelzenbach, C. J. Stapels, R.-M. Larimer, E. B. Norman, and A. Piechaczek, *ibid.* **76**, 034319 (2007); C. W. Reich, Nucl. Data Sheets **110**, 2257 (2009).

[56] WWW Table of Atomic Masses; http://ie.lbl.gov/toi2003/MassSearch.asp.

[57] F. Iachello, Phys. Rev. Lett. **85**, 3580 (2000).

[58] T. Otsuka and M. Sugita, Phys. Rev. Lett. **59**, 1541 (1987).

[59] S. Mukhopadhyay, M. Scheck, B. Crider, S. N. Choudry, E. Elhami, E. Peters, M. T. McEllistrem, J. N. Orce, and S. W. Yates, Phys. Rev. C **78**, 034317 (2008); A. A. Sonzogni, Nucl. Data Sheets **103**, 1 (2004); T. Ahn, L. Coquard, N. Pietralla, G. Rainovski, A. Costin, R. V. F. Janssens, C. J. Lister, M. Carpenter, S. Zhu, and K. Heyde, Phys. Lett. B **679**, 19 (2009); Yu. Khazov, A. A. Rodionov, S. Sakharov, and B. Singh, Nucl. Data Sheets **104**, 497 (2005); A. Gade, I. Wiedenhöver, H. Meise, A. Gelberg, and P. von Brentano, Nucl. Phys. A **697**, 75 (2002); L. Coquard *et al.*, Phys. Rev. C **80**, 061304(R) (2009); M. Kanbe and K. Kitao, Nucl. Data Sheets **94**, 227 (2001); S. Pascu, Gh. Cata-Danil, D. Bucurescu, N. Marginean, N. V. Zamfir, G. Graw, A. Gollwitzer, D. Hofer, and B. D. Valnion, Phys. Rev. C **79**, 064323 (2009); J. Katakura and Z. D. Wu, Nucl. Data Sheets **109**, 1655 (2008); T. Tamura, *ibid.* **108**, 455 (2007); K. Kitao, Y. Tendow, and A. Hashizume, *ibid.* **96**, 241 (2002); K. Kitao, *ibid.* **75**, 99 (1995).

[60] R. F. Casten and N. V. Zamfir, Phys. Rev. Lett. **85**, 3584 (2000).

[61] K. Heyde, P. Van Isacker, M. Waroquier, and J. Moreau, Phys. Rev. C **29**, 1420 (1984).

[62] I. Stefanescu *et al.*, Nucl. Phys. A **789**, 125 (2007).

[63] B. Sorgunlu and P. Van Isacker, Nucl. Phys. A **808**, 27 (2008).

[64] E. Williams *et al.*, Phys. Rev. C **74**, 024302 (2006); B. Singh, Nucl. Data Sheets **109**, 297 (2008); D. De Frenne, *ibid.* **110**, 1745 (2009); J. Blanchot, *ibid.* **108**, 2035 (2007); J. Srebrby *et al.*, Nucl. Phys. A **766**, 25 (2006); D. De Frenne and A. Negret, Nucl. Data Sheets **109**, 943 (2008); J. Blachot, *ibid.* **91**, 135 (2000); D. De Frenne and E. Jacobs, *ibid.* **89**, 481 (2000).